eLife

Reviewed Preprint
v1 • May 28, 2026
Not revised

For correspondence:
wfli@nju.edu.cn
wangwei@nju.edu.cn

Competing interests: No competing interests declared

Reviewing editor: Bin Zhang, Massachusetts Institute of Technology, United States

Role of desolvation on biomolecular liquid-liquid phase separation

Kai Zhang[1,2], Zhiyu Peng[1], Wenfei Li[1,2,3] ✉, Wei Wang[1] ✉

[1]Department of Physics, National Laboratory of Solid State Microstructure, Nanjing University, Nanjing, China • [2]Wenzhou Key Laboratory of Biophysics, Wenzhou Institute, University of Chinese Academy of Sciences, Wenzhou, China • [3]Jiangsu Key Laboratory for Cardiovascular Information and Health Engineering Medicine, Department of Cardiology, Nanjing Drum Tower Hospital, Medical School, Nanjing University, Nanjing, China

eLife Assessment

This manuscript presents a **valuable** and timely contribution by incorporating desolvation barriers into coarse-grained models of biomolecular condensates. The findings are **convincing**, supported by a clear physical model and systematic simulations showing effects on phase behavior, packing, and dynamics. Some clarification and broader context would improve the manuscript, but it provides a foundation that will be of use for developing more realistic coarse-grained interaction schemes.

https://doi.org/10.7554/eLife.111124.1.sa3

Abstract

Biomolecular condensates play essential roles in cellular organization and are implicated in diverse pathological processes. Their formation is driven by liquid-liquid phase separation (LLPS), a process that requires coordinated multistep desolvation of biomolecular chains and multivalent inter-chain interactions. Although coarse-grained (CG) models with implicit solvent are widely used to probe LLPS thermodynamics and kinetics, they typically neglect explicit desolvation energetics, limiting their accuracy and mechanistic interpretability. Here, guided by all-atom simulations and experimental measurements, we develop a CG model that incorporates residue-level desolvation terms directly into the energy function and apply it to investigate LLPS of intrinsically disordered proteins. Incorporating explicit desolvation reshapes the phase diagram, yielding improved predictions of dense-phase packing density. Strikingly, we uncover a linear relationship between the temperature gap (simulation temperature relative to the critical point) and the extent of conformational compaction accompanying the dilute-to-dense phase transition, a result further supported by theoretical analysis. We also find that desolvation barriers accelerate early-stage coarsening dynamics while slowing chain mobility within mature condensates, whereas solvent-separated contact interactions exert the opposite effects. Together, this framework enables efficient and explicit treatment of desolvation in CG simulations and reveals how desolvation energetics shape both the thermodynamic landscape and kinetic property of biomolecular LLPS.

Introduction

Biomolecular condensates formed through Liquid-liquid phase separation (LLPS) are increasingly recognized as fundamental regulators of diverse cellular processes, including stress responses Van Der Lee et al. (2014); Feric et al. (2016); Shin and Brangwynne (2017); Boeynaems et al. (2018); Burke et al. (2015); Biamonti and Vourc'h (2010); Riback et al. (2017), cellular signaling Wippich et al. (2013); Su et al. (2016), gene expression regulation Morimoto and Boerkoel (2013); Hnisz et al. (2017), and chromatin organization Strom et al. (2017). Dysregulation of condensate formation, in contrast, has been implicated in a wide range of human diseases, most notably cancer and numerous neurodegenerative disorders Molliex et al. (2015);

Patel et al. (2015); Boeynaems et al. (2018); Conicella et al. (2016); Osterburg and Dötsch (2022). Intrinsically disordered proteins (IDPs), which lack stable tertiary structures and often contain multivalent interaction motifs, are key molecular drivers of LLPS Molliex et al. (2015); Uversky et al. (2015); Zhou et al. (2018); Dignon et al. (2020); Elbaum-Garfinkle et al. (2015). Understanding the molecular principles governing IDP-mediated LLPS is therefore essential for elucidating the mechanisms underlying both physiological condensate function and pathological phase transitions. A central yet incompletely understood aspect of LLPS is the multi-step desolvation of biomolecular chains as they transition from a homogeneously dispersed solution to a condensed phase. How this desolvation energetics contributes to the thermodynamics and kinetics of LLPS remains a major open question.

Because experimentally characterizing the microscopic molecular events of LLPS at sub-molecule level is still challenging for most experimental assays, a broad spectrum of computational approaches has been developed to characterize biomolecular phase separation. These range from mean-field Flory (1942); Huggins (1941) and random-phase-approximation polymer theories Lin et al. (2017); Lin and Chan (2017); McCarty et al. (2019) to diverse molecular simulation frameworks based on atomistic or coarse-grained (CG) force fields Dignon et al. (2018b,a); Davtyan et al. (2012); De Jong et al. (2013); Baul et al. (2019). Although all-atom molecular dynamics (MD) simulations can capture the microscopic processes of biomolecules with unprecedented temporal and spatial resolutions, they become computationally prohibitive when applied to biomolecular phase separation involving large number of protein chains. This challenge has motivated the development of CG models that reduce computational cost while retaining the essential physicochemical features governing phase behavior. These CG frameworks include the sticker-and-spacer paradigm and its lattice Monte-Carlo implementation LASSI Harmon et al. (2017); Ruff et al. (2021); Choi et al. (2019), the hydrophobicity-scale (HPS) family and its refinements Dignon et al. (2018b,a); Regy et al. (2021); Dannenhoffer-Lafage and Best (2021), and Mpipi, which explicitly incorporates cation-π interactions Joseph et al. (2021). Advanced multiscale models have also been pioneered to predict the coupled phase behavior of IDPs and chromatin with remarkable accuracy Espinosa et al. (2020). Higher-resolution or experimentally fine-tuned CG force fields (e.g., AWSEM-IDP Wu et al. (2018), Martini3 Zhang et al. (2023); Souza et al. (2021), COCOMO Valdes-Garcia et al. (2023); Jussupow et al. (2025), AICG2+ Li et al. (2014); Bian et al. (2024), and SIRAH Darré et al. (2015)) further capture hydrogen bonding, secondary-structure propensity, and sequence-dependent packing. Notably, the maximum entropy optimized force field (MOFF) integrates maximum entropy biasing and energy landscape theory, successfully predicting the experimental dimensions and macroscopic phase separation of both ordered and disordered proteins Latham and Zhang (2019, 2021). More recently, Tesei et al. introduced the CALVADOS model, which optimizes residue-specific interaction parameters within the HPS framework using SAXS and paramagnetic relaxation enhancement (PRE) data across a large IDP dataset Tesei et al. (2021); Tesei and Lindorff-Larsen (2022); Tesei et al. (2024), thereby improving the accuracy and transferability of CG models for predicting IDP conformations and LLPS behavior.

Despite these advances, most residue-level CG models rely on implicit solvent representations. This simplification neglects the contribution of water molecules in mediating inter-residue interactions, which can be crucial for the thermodynamics and kinetics of biomolecular folding and phase transitions Cheung et al. (2002); Liu and Chan (2005); Karanicolas and Brooks III (2002); Tarus et al. (2006); Wu et al. (2011b). In particular, the desolvation penalty associated with electrostatic and hydrophobic interactions exhibits marked differences between implicit and explicit solvent representations Salari and Chong (2012); Wu et al. (2011a). More importantly, conventional implicit-solvent CG models cannot capture the multi-step desolvation events that accompany the transition from a dilute solution to a dense condensate in LLPS. Recent theoretical and experimental studies highlight that water reorganization and solvent-mediated entropy changes are not merely passive consequences of LLPS but active driving forces that shape condensate stability, internal structure, and dynamics Mukherjee and Schäfer (2023); Mukherjee et al. (2024); Li and Hou (2023). Nevertheless, implicit-solvent CG models remain widely used because they strike an effective balance between computational efficiency and residue-specific

resolution. Incorporating explicit desolvation physics into such models thus represents a particularly promising strategy for enhancing their physical realism without sacrificing tractability in LLPS simulations. Notably, residue-level desolvation terms have already been successfully employed in protein folding studies Cheung et al. (2002); Liu and Chan (2005); Ferguson et al. (2009); Chen and Chan (2014); Zhang and Chan (2010); Karanicolas and Brooks III (2002); Gasic and Cheung (2020); Camilloni et al. (2016). Within a structure-based modeling framework, Cheung et al. introduced a desolvation barrier separating the direct-contact minimum from the solvent-separated minimum in pairwise residue-residue potentials Cheung et al. (2002). Simulations demonstrated that this minimalist desolvation model captures water-expulsion events during the final stages of folding. Chan and colleagues further showed that incorporating a desolvation barrier markedly enhances folding cooperativity Liu and Chan (2005); Ferguson et al. (2009); Chen and Chan (2014); Zhang and Chan (2010). These previous successes provide a strong foundation for the explicit implementation of desolvation effect in coarse-grained models to more realistically investigate the critical contribution of desolvation in LLPS.

In this study, we advance the coarse-grained modeling of biomolecular LLPS by explicitly incorporating desolvation terms into the energy function of CG model. By performing molecular simulations, we systematically investigate how desolvation influences phase behavior, thermodynamic properties, and the microscopic dynamics underlying condensate formation as well as the internal dynamics of the equilibrated dense phase. We further optimize the desolvation parameters using all-atom MD simulations and experimental R_g measurements, yielding a refined framework for realistically modeling sequence-dependent phase behavior of biomolecules at microscopic resolution.

Results

Explicit modeling of desolvation effects in coarse-grained models

In order to elucidate the role of water molecules in mediating inter-residue interactions, we first performed all-atom MD simulations with explicit solvent for a set of amino acid analogues and computed the potential of mean force (PMF) along inter-residue distances (r). Methane, methanol, acetate ion, ammonium ion and methanamide were chosen to represent non-polar, polar, negatively charged, positively charged, and backbone-like residues, respectively. These amino acid analogues cover the key features of most amino acid types. The simulations were performed under ambient conditions (300 K and 1 atm), and the sampled snapshots were then analyzed to determine the inter-molecule distances and the corresponding PMF profiles. Additional simulation details are provided in the Methods section.

Figure 1A shows the PMF profile for the methane system. In addition to the deep potential well corresponding to the direct contact between two methane molecules ($r \sim 4$ Å), there exists a shallow potential well at larger distance ($r \sim 7$ Å). This shallow minimum arises from transient, solvent-separated pseudo contacts between the solute residues, hereafter referred to as solvent-separated contact. To form a direct contact between the solutes, the water molecules mediating the solvent-separated contacts need to be excluded, which leads to a desolvation barrier between the two potential wells. Similar features have been reported in previous all-atom MD simulations Liu and Chan (2005). The PMF profiles extracted based on the simulations for other amino acid analogues exhibit the same overall shape (Figure 1B and Figure 1—figure supplement 1), but the positions of the direct-contact minimum (r_{dc}), the solvent-separated minimum (r_{ss}), and the desolvation barrier (r_b) vary depending on the analogue molecules. The depths of the two potential wells (ϵ and ϵ_{ss}) and the height of the desolvation barrier (ϵ_b) likewise differ across analogue pairs. The desolvation effect is also intrinsically modulated by solvent polarity, which can be realized experimentally by changing ionic strength or adding cosolvents. To elucidate this relationship, we performed additional simulations of the methane system in water with systematically varied polarity. For simplicity, the solvent polarity was tuned by uniformly scaling the partial charges of the hydrogen and oxygen atoms in the water molecules. This approach directly modulates the strength of solvent-solvent electrostatic interactions, which in turn dictates

the stability of the hydration shell surrounding the solute. We compared the standard water model (1.0× charges) with reduced-polarity models (0.9× and 0.8× charges) (Figure 1A). The results reveal that a reduction in solvent polarity leads to a simultaneous decrease in the height of the desolvation barrier and the depth of the solvent-separated minimum. These observations underscore the importance of explicitly modeling the desolvation energetics and exploring the effects of different desolvation strengths on the thermodynamics and kinetics of protein LLPS.

In this work, we introduce desolvation terms into the HPS model developed by Dignon et al. (2018b). In this framework, each residue is simplified to a single spherical bead. The HPS energy function includes the bonded term and nonbonded term (see Materials and methods). The nonbonded term is described by the short-range pairwise interactions and long-range electrostatic interactions. To account for the desolvation effect, we added two Gaussian functions centered at r_{b} and r_{ss} to represent the desolvation barrier and the solvent-separated contact, respectively. The resulted nonbonded energy function with desolvation effect is given by

$$\begin{aligned} U(r) &= \Phi(r,\epsilon,\lambda,\sigma) + G_{\mathrm{b}}\left(r,\epsilon_{\mathrm{b}},r_{\mathrm{b}},\sigma_{\mathrm{b}}\right) - G_{\mathrm{ss}}\left(r,\epsilon_{\mathrm{ss}},r_{\mathrm{ss}},\sigma_{\mathrm{ss}}\right) \\ &= \Phi(r,\epsilon,\lambda,\sigma) + \epsilon_{\mathrm{b}}\exp\left[-\frac{\left(r-r_{\mathrm{b}}\right)^2}{2\sigma_{\mathrm{b}}^2}\right] - \epsilon_{\mathrm{ss}}\exp\left[-\frac{\left(r-r_{\mathrm{ss}}\right)^2}{2\sigma_{\mathrm{ss}}^2}\right]. \end{aligned} \tag{1}$$

Here $\Phi(r, \epsilon, \lambda, \sigma)$ denotes the nonbonded term in the original HPS model energy function Dignon et al. (2018b). The parameters λ and σ correspond to the hydrophobicity scale values and effective bead sizes, respectively, for the 20 amino acids.

We first employ a homopolymer protein model with a chain length of 50 residues to illustrate the desolvation effect. For each residue, we use the parameter set extracted by averaging among the intrinsically disordered proteins in the Disprot dataset Aspromonte et al. (2024), which gives an amino acid mass of m_{residue} = 110 amu (atomic mass unit), a hydrophobicity parameter λ = 0.640, and an effective bead size σ = 0.536 nm. The parameter ϵ_{b} governs the height of desolvation barrier associated with expelling water molecules between residues, whereas ϵ_{ss} determines the depth of the local minimum corresponding to a solvent-separated contact. Together, these parameters shape the desolvation potential and modulate the energetic cost of excluding hydration water. By tuning the parameter values of ϵ_{ss} and ϵ_{b}, we generate energy functions with varying degree of desolvation contributions (Figure 1C), enabling systematic investigation of how desolvation influences the phase behavior and thermodynamics of IDPs. Unless explicitly stated otherwise, all thermodynamic quantities are reported in terms of a reduced temperature, defined as $T^* = k_{\mathrm{B}}T/\epsilon$. Here, ϵ denotes the characteristic interaction energy scale of the system, which is set to ϵ = 0.2 kcal/mol following the convention of the HPS model Dignon et al. (2018b).

Thermodynamic impact of desolvation on the phase diagram

To capture the essential physics of IDP phase separation, we employed a coarse-grained model of 125 homopolymer chains using a slab simulation protocol (Methods). As a control, we first performed molecular dynamics simulations within the HPS model framework without considering the desolvation terms across a range of temperatures (Figure 2A-C). Representative snapshots clearly illustrate the transition from a homogeneous solution to a stable condensate as the temperature decreases (Figure 2B). We extracted time-averaged density profiles along z-axis to identify coexisting dense and dilute phases and thereby constructed the binodal curve (Figure 2A,C), which reproduces phase behaviors reported in previous molecular simulation studies Dignon et al. (2018b). We then repeated the slab simulations while explicitly including desolvation energetics with varying ϵ_{b} and ϵ_{ss} to investigate how desolvation reshapes the phase diagram and condensate structure.

To elucidate how desolvation regulates thermodynamics of LLPS, we systematically mapped phase diagrams under varying desolvation parameters (Figure 2D and E). Increasing the desolvation barrier ϵ_{b} monotonically lowers the critical temperature T_c^* (Figure 2D), suggesting a reduced phase separation propensity. Analysis of residue-residue radial distribution functions showed that higher ϵ_{b} suppresses density distribution in the barrier region, suggesting an entropic

Figure 1. Desolvation effect of inter-molecular interactions.

(A) Potential of mean force along the inter-molecule distances for the amino acid analogues from all-atom MD simulations with different water polarity. (B) Schematic diagram of desolvation effect. (C) Pair-wise energy function incorporating desolvation terms. Different curves correspond to different desolvation parameters.

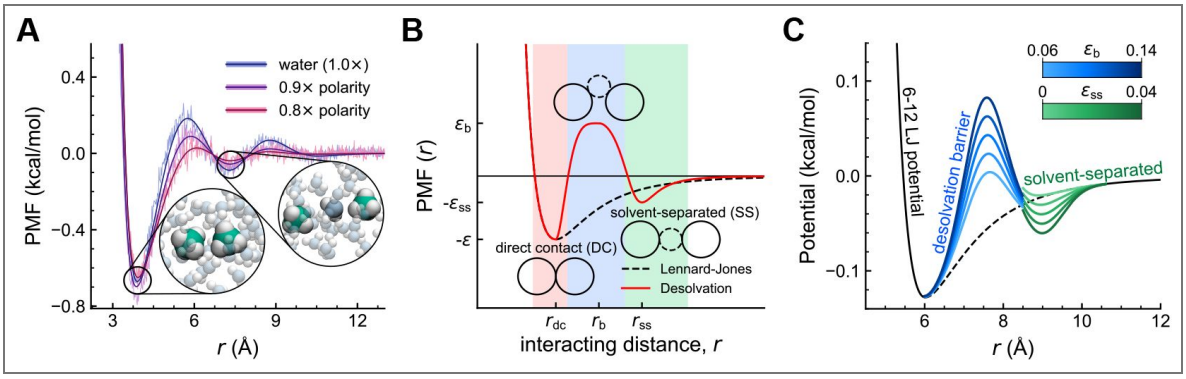

Figure 2. Thermodynamic regulation and microscopic mechanisms of desolvation-mediated phase separation.

(A) Baseline phase diagram of the poly-50 system using the standard HPS model. (B) Representative simulation snapshots visualizing the transition from a stable condensate ($T^* = 2.58$) to a near-critical state ($T^* = 2.98$) and a homogeneous solution ($T^* = 3.18$). (C) Time-averaged density profiles along the z-axis identifying the coexisting dense and dilute phases. (D, E) Macroscopic phase boundaries under varying desolvation barrier heights ϵ_b (D) and solvent-separated potential depths ϵ_{ss} (E). Insets show the monotonic dependence of T_c on the respective parameters. The lower schematics highlight the distinct thermodynamic drivers: entropic penalty (ϵ_b) versus enthalpic stabilization (ϵ_{ss}). (F, G) Renormalized phase behavior plotted against normalized temperature T^*/T_c for varying ϵ_b (F) and varying ϵ_{ss} (G).

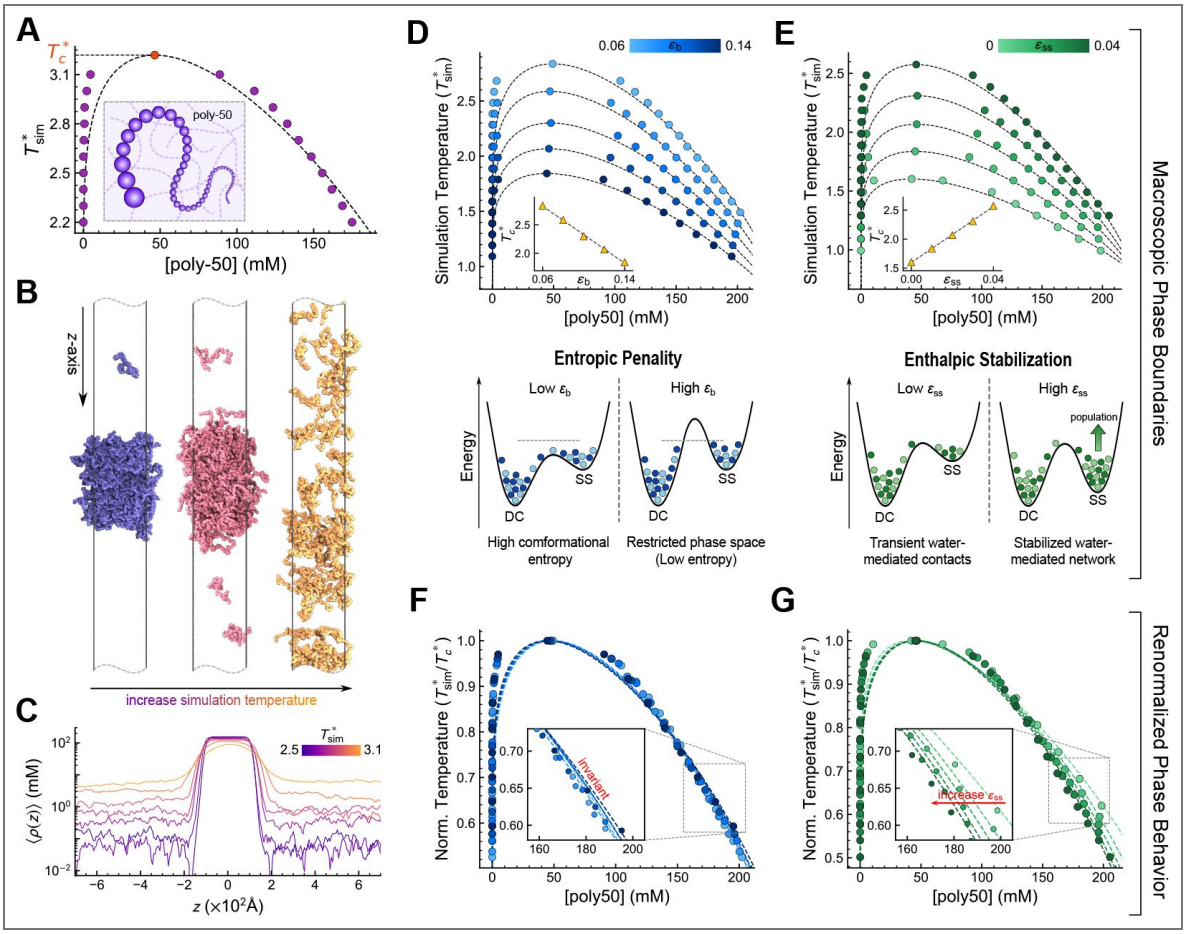

penalty that restricts the conformational volume available for residue-residue association (Figure 2—figure supplement 1C). By contrast, deepening the solvent-separated well ϵ_{ss} elevates T_c^* (Figure 2E), which is attributed to an enthalpic stabilization driven by water-mediated bridging as shown by the enhanced population of solvent-separated configurations (Figure 2—figure supplement 1D). These opposing effects, entropic restriction versus enthalpic gain, suggest that the desolvation potential emerges as a key thermodynamic regulator that tunes macroscopic phase behavior via the balance of conformational entropy and solvent-mediated enthalpy (lower panels of Figure 2D and E).

Because the critical temperature is an intrinsic, sequence-specific property of a given system, it is also important to examine how desolvation strength alters the overall shape of the phase diagram when T_c^* is held constant. To do so, we rescaled the temperature axis by T_c^*, which effectively normalizes overall energetic strength and isolates desolvation-specific effects on the phase boundary. For the desolvation models with different barrier height ϵ_b, the normalized binodal curves nearly overlap (Figure 2F). By contrast, varying the solvent-separated well depth ϵ_{ss} results in distinct deviations in the density of the condensed phase (Figure 2G). Specifically, stronger water-mediated interactions lower equilibrium density by biasing the ensemble toward configurations with larger inter-residue separations (Figure 2—figure supplement 1E, F). Thus, solvent-separated interactions directly regulate molecular packing and, by introducing hydrated configurations, prevent artificial over-compaction as typically encountered in coarse-grained models with implicit solvent. These results suggest that explicitly including desolvation enables coarse-grained models to more faithfully capture the physicochemical structure of biological condensates.

Conformational modulation by desolvation in dense and dilute phases

We next investigate how desolvation modulates the conformational distribution of IDPs across dilute and condensed phases. To quantify the global chain dimensions, we calculated the radius of gyration (R_g) as a primary structural metric. The resulting R_g distributions for protein chains in both phases are presented in Figure 3B and C. Notably, the protein chains adopt more compact conformations in the dilute phase (smaller $\langle R_g \rangle$), whereas those in the condensed phase exhibit more extended conformations (larger $\langle R_g \rangle$). This conformational expansion upon condensation reflects a transition from the intra-chain dominated interactions to the inter-chain dominated interactions as typically encountered during phase of separation of IDPs Dignon et al. (2018b); Wei et al. (2017); Hazra and Levy (2021). Within the condensed phase, protein chains preferentially form inter-chain contacts that lower the free energy of the system, which compensate for the entropic cost associated with reduced translational and conformational freedom. The R_g distributions also suggest that chain conformations in the dilute phase are much more sensitive to variations in desolvation parameters than in the condensed phase (Figure 3B and C). Consequently, the variation in the conformational difference $\Delta R_g = R_g^{\mathrm{dense}} - R_g^{\mathrm{dilute}}$ arises predominantly from the conformational changes of isolated chains in the dilute phase. Physically, ΔR_g captures the transition from intramolecular-dominated collapse in the dilute phase to intermolecular-mediated expansion in the dense phase, thus serving as a metric for the relative strength of inter-chain versus intra-chain interactions.

To further elucidate the thermodynamic implications of desolvation-modulated conformations, we analyzed the relationship between the conformational shift ΔR_g and the thermal distance to the critical point, defined as $T_c^* - T_{\mathrm{sim}}^*$. Strikingly, data from all simulated systems nearly collapse onto a single curve, revealing a strong universal correlation between the magnitude of conformational change and the thermal distance to the phase transition point (R^2 = 0.942, Figure 3D). This result demonstrates that the conformational response to phase separation is governed fundamentally by how far the system resides thermally from the critical point, irrespective of the specific microscopic desolvation energetics.

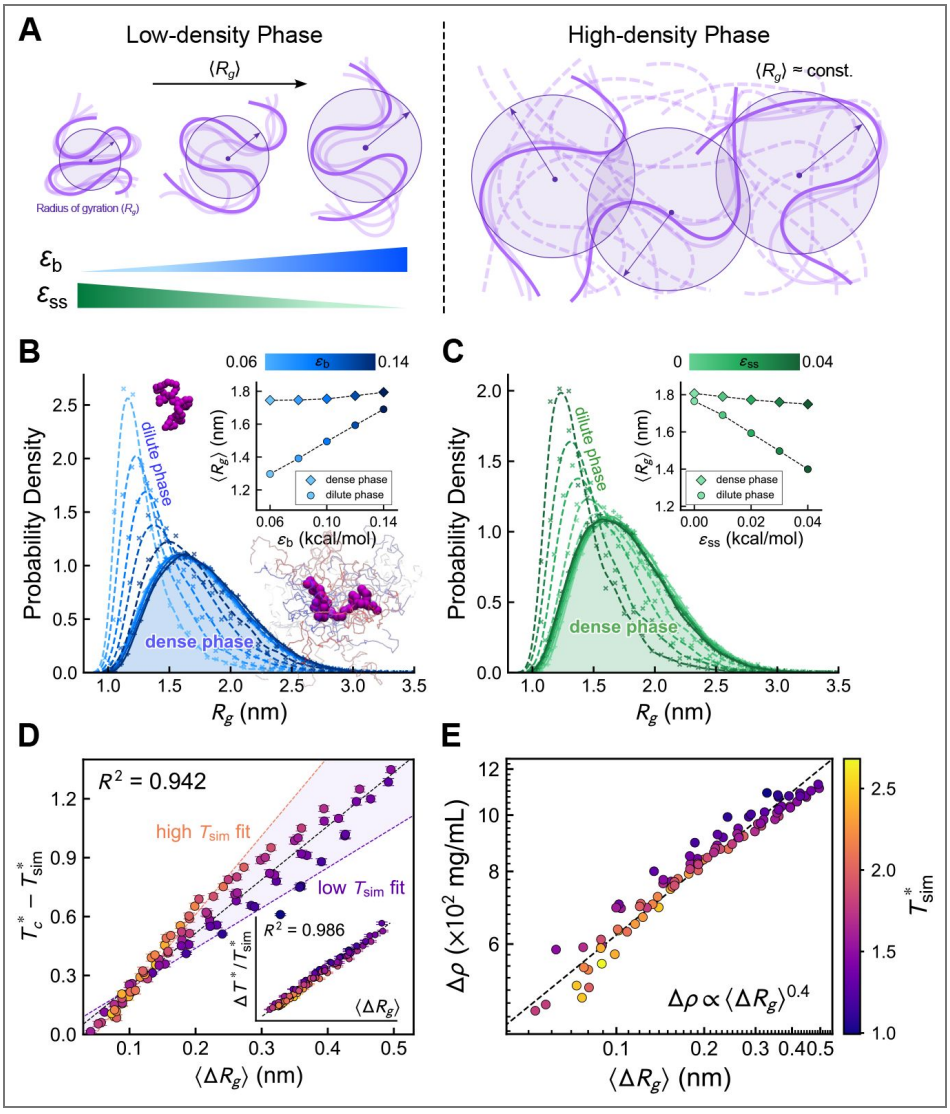

Figure 3. Effect of desolvation on protein conformations.

(A) Schematic illustration of the conformational distributions of the protein in the high-and low-density phases under different desolvation parameters. (B-C) Distribution of R_g with different ϵ_b (B) and ϵ_{ss} (C) at $T^*_{sim} = 1.59$. The solid and dashed lines represents the results in the condensed and dilute phases respectively. The inset illustrates the mean value of R_g as a function of desolvation parameters. (D) Correlation between temperature difference $(T^*_c - T^*_{sim})$ and the averaged R_g difference between two phases. The purple and yellow dashed lines represent linear fits to the data obtained at low simulation temperatures $(T^*_{sim} < 1.2)$ and high-temperature $(T^*_{sim} > 2.4)$ regimes respectively. The inset displays the improved linearity obtained when the temperature difference is normalized by the simulation temperature, $(T^*_c - T^*_{sim})/T^*_{sim}$. (E) Correlation between the density difference and R_g difference in the two phases with varying temperatures and desolvation parameters. The plot was shown in a log-log scale.

We rationalize this observation using the Flory-Huggins theory Huggins (1942); Flory (1942) as a bridge between the macroscopic thermal distance and the microscopic interaction strength. In this theoretical framework, the thermodynamic state is defined by the interaction parameter $\chi = \epsilon_{\text{eff}}/(k_B T)$, where ϵ_{eff} represents the effective pairwise energy scale specific to each desolvation model Flory (1953). By invoking the critical condition $\epsilon_{\text{eff}} = k_B T_c \chi_c$, where χ_c is a universal constant determined solely by the fixed chain length N, we eliminate the system-specific energy scale ϵ_{eff}.

This substitution reveals that the deviation from the critical interaction parameter scales strictly with the normalized thermal distance, $[\chi(T_{\text{sim}}) - \chi_c] \propto (T_c - T_{\text{sim}})/T_{\text{sim}}$. The thermodynamic driving force χ can then be related to the structural observable ΔR_g. Since ΔR_g captures the structural transition from a intrachain-interaction dominated state in the dilute phase to an interchain-interaction dominated state in the dense phase, we posit that this conformational shift scales linearly with the excess interaction strength, expressed as $\Delta R_g \propto [\chi(T_{\text{sim}}) - \chi_c]$. Combining these relations leads to a theoretical prediction where the thermal distance is related to the conformational change scaled by the simulation temperature

$$T_c - T_{\text{sim}} \propto T_{\text{sim}} \Delta R_g. \tag{2}$$

This derivation explains the approximate linearity observed in Figure 3D while also accounting for the systematic deviation caused by the temperature coefficient, which is evident from the varying slopes between low-temperature and high-temperature data points. To validate our theoretical derivation and the underlying linear response assumption, we removed this temperature factor and replotted the data against the normalized thermal distance $\left(T_c^* - T_{\text{sim}}^*\right)/T_{\text{sim}}^*$. As shown in the inset of Figure 3D, this operation yields a nearly perfect linear relationship ($R^2 = 0.986$). This statistical enhancement confirms the above argument that ΔR_g scales linearly with the interaction distance $\chi - \chi_c$, thereby establishing that the conformational response of IDPs is intrinsically dictated by the thermal distance from the critical point.

We further show the relationship between the phase density difference ($\Delta\rho = \rho_{\text{dense}} - \rho_{\text{dilute}}$) and the conformational difference (ΔR_g) between coexisting phases in Figure 3E. From the previously established proportionality $T_c - T_{\text{sim}} \propto \Delta R_g$, one can relate the density contrast $\Delta\rho$ to ΔR_g through the critical-scaling relation by $\Delta\rho = A(T_c - T)^{\beta}$ (Equation (6)), where β is the critical exponent. Substituting the linear relation $T_c - T_{\text{sim}} \propto \Delta R_g$ into this expression yields $\Delta\rho \propto (\Delta R_g)^{\beta}$. On logarithmic scales, a clear power-law dependence emerges (Figure 3E), with $\Delta\rho \propto \Delta R_g^{0.4}$, which is consistent with our theoretical expectation. The fitted exponent (≈ 0.4) is in reasonable agreement with the theoretical critical exponent $\beta = 0.325$ based on 3D Ising model Rowlinson and Widom (2013). Collectively, these results reveal a fundamental coupling between microscopic conformational reorganization and macroscopic packing density during biomolecular condensation, underlying conformational reorganization as a structural signature of the phase transition.

Dynamic consequences of desolvation in phase separation

Beyond governing thermodynamic phase boundaries and conformational distribution, the desolvation potential fundamentally reshapes the dynamical landscape of IDP condensates. The interplay between inter-chain interactions and solvent exclusion not only dictates the stability of the dense phase but also modulates the transport properties within the condensate and the macroscopic kinetics of phase separation. To probe the chain mobility within the dense phase, we employed a strategy analogous to fluorescence recovery after photobleaching (FRAP) experiments following prior molecular dynamics simulation work Yamada and Takada (2023), tracking the spatiotemporal evolution of specific chains initially localized at the slab center (Figure 4A and B). For the standard HPS model without desolvation, the tagged chains achieve a uniform distribution that matches the equilibrium density profile within 50 ns (Figure 4B). This rapid relaxation confirms a liquid-like nature of the condensate. Incorporating desolvation effects

significantly slows down the relaxation process. The spatial distribution of tracked chains remains biased toward the initial center position after 50 ns and requires a prolonged timescale (~ 150 ns) to fully equilibrate. This slowing down suggests that desolvation introduces additional roughness to the energy landscape that govern molecular transport.

To more rigorously quantify this mobility, we computed the time-averaged mean squared displacement (TAMSD) Metzler et al. (2014) for chains within the slab. The chain motion exhibits sub-diffusive scaling, TAMSD = $K \cdot \Delta t^{\alpha}$, with a characteristic exponent $\alpha \approx 0.91$ (Figure 4A, bottom right panel). This deviation from normal diffusion ($\alpha = 1$) primarily reflects the viscoelastic nature of the crowded condensed phase with multi-valent dynamic interaction network, where chain motion is hindered by molecular crowding and chain constraints. At extended lag times, the TAMSD curves naturally plateau as they approach the geometric limit imposed by the slab thickness. Notably, our observed exponent is comparable to simulation results reported for protein diffusion in three-dimensional condensates ($\alpha \approx 0.85$) Watanabe et al. (2025), consistently highlighting the restricted nature of chain dynamics within dense phase. Given the robustness of α across different interaction parameters, we utilized the generalized diffusion coefficient K to characterize the transport rates.

The modulation of the diffusion coefficient reveals a clear dependence on the interaction parameters (Figure 4C). At a constant temperature, K increases with the desolvation barrier ϵ_b and decreases with the well depth ϵ_{ss} (Figure 4C, left panels). These seemingly divergent trends are effectively unified by the packing state of the condensate. As illustrated in Figure 4C (right panel), the diffusion coefficient is predominantly correlated with the bulk density (ρ_{dense}), accompanied by a secondary temperature modulation, where higher temperatures provide a modest increase in mobility beyond the baseline packing constraints. Consistent with the density trends established in Figure 2D and E, a higher ϵ_{ss} promotes tighter packing, increasing the effective friction, whereas a higher ϵ_b prevents close contacts, creating greater free volume that facilitates diffusion. These results indicate that, at a fixed absolute temperature, macroscopic density serves as the primary determinant of chain mobility.

However, this density-dominated view is incomplete because it convolutes intrinsic energy landscape features with thermodynamic state shifts. Since variations in ϵ_b and ϵ_{ss} significantly alter the critical temperature, comparisons made at a constant absolute temperature inherently involve systems positioned at different thermodynamic quench depths, defined as the normalized temperature deviation from the critical point. This highlights the distinct thermodynamic driving forces for different systems. To disentangle the intrinsic influence of the desolvation potential from these thermal effects, we renormalized our analysis. First, we scaled the simulation temperature by the critical temperature of each system and utilized the ratio T^*_{sim}/T^*_c as the control parameter for quench depth, noting that a lower value corresponds to a deeper quench. This ensures the thermodynamic equivalence across different interaction parameters. Second, to factor out the inherent linear dependence of Brownian motion on temperature where the diffusion rate scales with k_BT, we defined a reduced diffusion coefficient $\tilde{K} = K/T$ as detailed in the Supplementary Information. In this renormalized frame, the intrinsic signature of the energy landscape emerges clearly (Figure 4D). At the same quench depth, where thermodynamic driving forces are comparable, a higher desolvation barrier ϵ_b (darker blue points) yields a lower reduced diffusion rate $\tilde{K}$. Crucially, this kinetic divergence becomes increasingly pronounced at deeper quenches (lower T^*_{sim}/T^*_c) but effectively vanishes near the critical point, indicating that the regulatory role of the intrinsic energy landscape amplifies as the system moves further from the critical point. Notably, the standard HPS model exhibits much faster intrinsic mobility (Figure 4 red triangles), confirming that neglecting specific desolvation energetics artificially smooths the energy landscape and leads to an overestimation of chain dynamics. The trend shown in Figure 4C and D uncovers the physical reality masked by density effects. Specifically, it reveals that while a higher ϵ_b loosens the macroscopic packing, it simultaneously roughens the microscopic energy landscape. The desolvation barriers increase the activation energy required for local chain rearrangement, thereby suppressing the intrinsic mobility. Thus, the chain

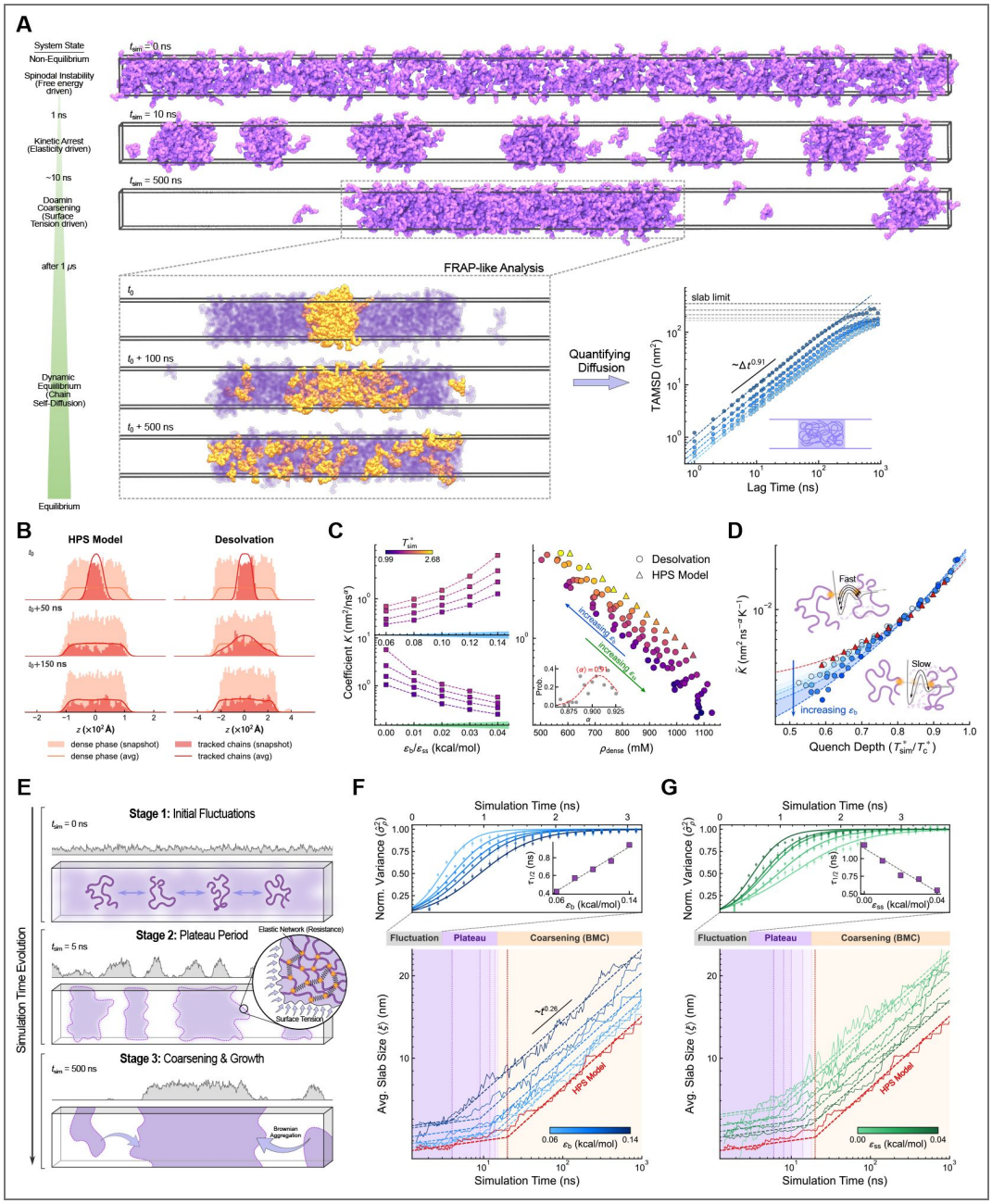

Figure 4. Desolvation-mediated modulation of diffusion and coarsening dynamics.

(A) Snapshots of spinodal decomposition and equilibrium chain diffusion. The top panels illustrate domain coarsening, while the bottom panels highlight self-diffusion of highlighted chains in the stable slab. The inset quantifies the chain mobility via TAMSD analysis. (B) Density profiles of biomolecules along the *z*-axis for the entire system (orange) and for the highlighted chains (red) at different time lags with and without desolvation. The solid curves represent normalized averages over 1 μs. (C) Diffusion coefficients as a function of the inter-chain desolvation strength (ϵ_b, ϵ_{ss}) and dense-phase densities (ρ_{dense}) at different temperatures. (D) Reduced diffusion coefficient $\tilde{K}$ versus quench depth for varying ϵ_b. The schematic inserts highlight the impact of energy landscape roughness on diffusion dynamics. (E) Schematic representation of the phase separation mechanism. The diagram depicts the transition from initial density fluctuations to late-stage growth, mediated by an intermediate plateau. The zoom-in view details the structural origin of the kinetic arrest arising from strong inter-chain interactions. (F, G) Kinetics of density fluctuations and domain growth. Top: Time evolution of the normalized density variance $\langle \hat{\sigma}_\rho^2 \rangle$ The inset shows the characteristic time $\tau_{1/2}$. Bottom: Growth of the average slab size $\langle \xi \rangle$ on a logarithmic scale. The timeline bar highlights the three distinct regimes: initial fluctuation, kinetic arrest (plateau), and late-stage coarsening via Brownian Motion Coalescence (BMC).

dynamics are governed by a hierarchy of mechanisms: macroscopic density sets the baseline mobility through free volume, while the roughness of the desolvation-mediated energy landscape imposes a fine-tuned kinetic constraint.

Desolvation modulated kinetic arrest of coarsening dynamics

Elucidating the molecular events during the early stage of phase separation is challenging experimentally. We therefore examine droplet-growth dynamics at the early stage of phase separation by performing molecular simulations with explicit consideration of desolvation effect. Initially, the system was equilibrated at a supercritical temperature ($T^* = 2.98$) for 10 ns to ensure a homogeneous distribution. The temperature was then quenched to $T^* = 1.79$, located deep within the two-phase coexisting region, to initiate spontaneous phase separation (Figure 4A). Visually, the system evolves from an initially uniform distribution into interconnected structures within 1 ns ~ 2 ns, which subsequently breaks up into discrete high-density domains along z-axis. Over time, these domains gradually coalesce into larger slabs, exhibiting the characteristic morphological evolution of spinodal decomposition Cahn and Hilliard (1958).

To quantify the phase separation kinetics, we adopted a two-stage metric strategy. In the early stage, where interfaces are diffusive, we monitored the normalized density variance ($\langle\langle\hat{\sigma}_\rho^2\rangle\rangle$, see Supplementary Information) derived from the instantaneous density profile $\rho(z)$ to track the growth rate of density fluctuations. As clear interfaces emerged, we switched to tracking the average slab size ($\langle\xi\rangle$), defining dense domains as continuous regions where $\rho(z)$ exceeds a threshold value (here the average system density was used as the threshold). To ensure statistical robustness, all kinetic metrics were averaged over six independent slab simulation replicas. The resulting kinetic profiles (Figure 4F and G) reveal two distinct regimes. First, immediately after the temperature quench, the system undergoes a rapid exponential growth in density variance (top panels). This behavior is characteristic of spinodal decomposition Cahn (1961). The results show that stronger effective attraction (higher ϵ_{ss} or lower ϵ_b) tends to accelerate these initial fluctuations. This is quantitatively evidenced by the monotonic decrease in the characteristic time scale $\tau_{1/2}$, defined as the time required to reach 50% of the maximum normalized variance. Second, in the late stage ($t > 10$ ns), the domain growth transitions into a coarsening regime following a power-law scaling $\langle\xi\rangle \sim t^\alpha$ with $\alpha \approx 0.26$ (Bottom panels). Theoretically, the Brownian motion coalescence (BMC) mechanism predicts an asymptotic scaling of $\alpha = 1/3$ Majumdar et al. (1994). Our observed exponent falls slightly below this theoretical value, likely due to the viscoelastic nature of the polymer solution. Specifically, the sub-diffusive dynamics of individual chains (TAMSD $\sim \Delta t^{0.91}$) inherently constrain the macroscopic domain diffusion Doi et al. (1988), thereby retarding the coarsening rate below the standard Brownian prediction.

Intriguingly, between the initial spinodal decomposition and the late-stage Brownian coalescence, we observed a distinct intermediate plateau regime where the domain growth is temporarily arrested. As shown in the slab size evolution (Figure 4F and G, bottom), the domain growth stalls for a distinct period before entering the late-stage scaling regime. This kinetic arrest is visually corroborated by the density profiles at 5 ns in Figure 4E, where distinct domains are observed to form but fail to fuse immediately. The quantitative analysis in Figure 4F and G further reveals that these domains persist as distinct entities for durations that vary significantly depending on the desolvation parameters. This phenomenon is consistent with the characteristics of viscoelastic phase separation Tanaka (2000). It suggests that strong inter-chain interactions within the dense phase form a transient network structure. While surface tension drives the fusion of domains, the internal structural connectivity generates a resistance to the necessary shape deformation, thereby delaying coalescence. Crucially, the plateau duration extends significantly in systems with higher ϵ_{ss} or lower ϵ_b. This trend corroborates our viscoelastic interpretation, suggesting that stronger inter-chain attractions reinforce the transient network, thereby effectively prolonging the kinetic arrest. This kinetic trap is particularly pronounced in the standard HPS model (red trajectories in Figure 4F and G), due to its relatively stronger pairwise attractions. The sensitivity of kinetic arrest of coarsening dynamics to desolvation

parameters underscores the explicit modeling of desolvation in coarse-grained model in order to achieve a more physically plausible molecular simulations of LLPS. Synthesizing these observations, Figure 4E provides a schematic illustration of the three-stage evolution. This diagram maps the progression of driving forces, highlighting the transition from the initial regime dominated by inter-chain interactions, to a final stage governed primarily by surface tension-driven coarsening.

Collectively, we presented a comprehensive analysis of the phase separation dynamics, bridging the microscopic diffusion of single chains to the macroscopic growth of condensed domains. Our analysis underlies the essential role of desolvation potential. Beyond modulating thermodynamic stability and conformational ensembles as discussed earlier, it acts as a critical regulator of phase separation dynamics.

Parameterization of desolvation model for IDPs

The results from the homopolymer model discussed above underscore the critical role of desolvation in regulating both the thermodynamics and dynamics of LLPS. Consequently, explicitly incorporating water-mediated interactions into residue-level coarse-grained models is essential for more realistically capturing the physics of protein phase separation. To this end, we developed a transferable parameterization strategy derived from all-atom simulations and validated it against experimental observables of IDPs.

Experimentally determining the desolvation parameters, specifically, the barrier height ϵ_b and the solvent-separated minimum depth ϵ_{ss}, remains challenging. To bridge this gap, we leveraged all-atom molecular dynamics simulations of amino acid analogues to extract the corresponding energy scales. Taking the depth of the direct-contact potential well (ϵ) as a reference scale, we expressed the desolvation parameters as $\epsilon_b = \alpha_b\epsilon$ and $\epsilon_{ss} = \alpha_{ss}\epsilon$. By fitting the PMF profiles obtained from all-atom simulations (Figure 1—figure supplement 1), we determined the coefficients α_b and α_{ss}. Notably, these coefficients were highly consistent across different pairs of amino acid analogues. For simplicity and transferability, we adopted the averaged values $\alpha_b = 0.33$ and $\alpha_{ss} = 0.06$ as the initial baseline for our coarse-grained model.

To evaluate the effectiveness of these physics-derived parameters, we first integrated them into the framework of the standard HPS model. While the HPS model performs remarkably well in capturing sequence-dependent properties of LLPS, previous studies have noted that parameters optimized solely against single-chain R_g can face challenges in transferability to the condensed phase, often leading to an overestimation of phase separation propensity (i.e., higher critical temperatures, T_c) Dignon et al. (2018b). We assessed the model performance on a dataset of 47 IDPs taken from Tesei et al. Tesei et al. (2021). The deviation of simulated single-chain R_g from experimental SAXS data was quantified by $\chi^2_{R_g} = [(R_{g,\mathrm{exp}} - R_{g,\,\mathrm{sim}})/\sigma_{\mathrm{exp}}]^2$, where σ_{exp} represents the experimental uncertainty. When the desolvation parameters derived from all-atom simulations ($\alpha_b = 0.33$, $\alpha_{ss} = 0.06$) were added to the HPS model without modifying its original ϵ, we observed a substantial improvement in conformational accuracy. The average discrepancy $\langle\chi^2_{R_g}\rangle$ decreased drastically from 1,082.27 (original HPS) to 85.88 (HPS-desolvation) (Figure 5B). This improvement indicates that introducing the desolvation terms effectively mitigates the over-compaction tendency of the original HPS model likely by the competition between direct and water-separated contacts.

We also incorporated the desolvation terms into CALVADOS2 Tesei and Lindorff-Larsen (2022), a force field whose hydrophobicity parameters (λ) were reparameterized using Bayesian optimization to reproduce experimental R_g and PRE data. Directly adding desolvation terms to CALVADOS2 led to substantial chain over-expansion $\left(\langle\chi^2_{R_g}\rangle = 643.30\right)$, reflecting the fact that CALVADOS2 is already finely tuned to reproduce experimental data through a top-down optimization procedure and the inclusion of additional desolvation terms is incompatible with its parameterization. To address this, we implemented a systematic optimization strategy in which the desolvation barrier height (ϵ_b), solvent-separated minimum depth (ϵ_{ss}), and the overall energy factor ϵ were scanned over broad parameter ranges to identify the parameter set that minimizes

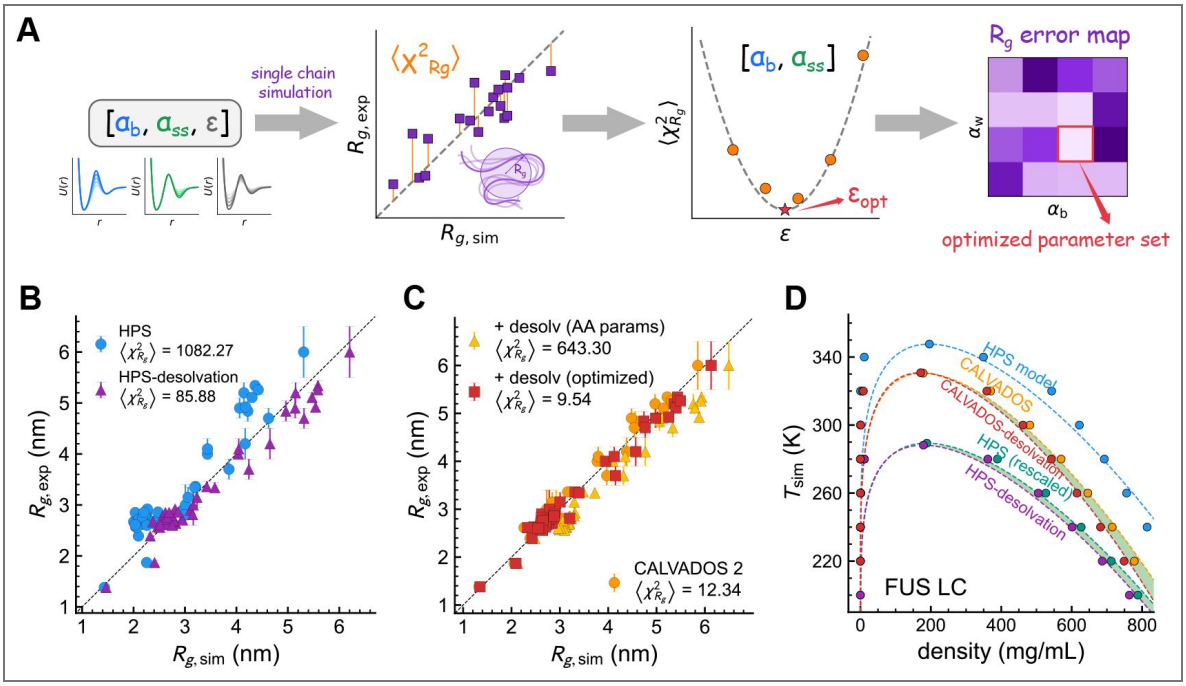

Figure 5. Parameterization of desolvation terms for the HPS model and CALVADOS2 model based on IDPs.

(A) Schematic workflow of the desolvation parameterization. (B) Correlation between experimental R_g and simulation R_g for the original HPS model (blue) and the revised HPS model with default desolvation scales (α = 0.33 and α = 0.06) (purple). The $\left\langle \chi^2_{R_g} \right\rangle$ for different models were also shown. (C) Correlation between experimental R_g and simulation R_g for the original CALVADOS2 model (orange), the revised CALVADOS2 model with default desolvation (yellow), and revised CALVADOS2 model with optimized desolvation (α_b = 0.3, α_{ss} = 0.03 and ϵ = 0.262 kcal/mol)(red). (D) Coexistence curves of FUS LC simulated with the original HPS model (blue), the revised HPS model with default desolvation scales (purple), the energy-rescaled HPS model (green), the default CALVADOS2 model (orange), and the revised CALVADOS2 model with optimized desolvation scales (red). The green shaded regions highlight the deviations of the desolvation models relative to the original frameworks.

deviations between simulated and experimental R_g values. The full optimization workflow is summarized in the flowchart in Figure 5A, and the resulting error landscapes are shown in Figure 5—figure supplement 1 and 2. The optimized parameter set (Table 1) achieved excellent agreement with experiments, reducing $\left\langle \chi^2_{R_g} \right\rangle$ to 9.54 (Figure 5C), which is comparable to the accuracy of the original CALVADOS2 model in describing R_g values.

We further probed the phase behavior using the FUS low-complexity domain (FUS LC) as a test case. Experimental observations indicate that the critical temperature is around 25 ˚C Burke et al. (2015). While the original HPS model overestimates this value with a critical temperature $T_c \sim$ 340 K, integrating the desolvation terms into the HPS framework (HPS-desolvation) results in a T_c of $\sim$ 290 K (Figure 5D) which aligns well with experimental observations. In addition to improving the prediction of the critical temperature, we observed that the desolvation model significantly mitigates the overestimation of condensate density common in implicit solvent coarse-grained simulations Regy et al. (2021); Benayad et al. (2020). In the CALVADOS2 framework, the inclusion of desolvation reduces the dense phase density while maintaining a critical temperature comparable to the original model (Figure 5D). Similarly, for the HPS model, when we rescaled the interaction strength ϵ to match the single-chain R_g and thereby align the critical temperature with the HPS-desolvation system (Figure 5—figure supplement 3), we observed the same behavior. Quantitatively, across both frameworks, the desolvation-modulated models consistently yield a packing density approximately 5% lower than the original models. This distinction underscores a limitation of standard Lennard-Jones potentials where a single parameter ϵ simultaneously controls chain dimension, critical temperature, and condensate density. In contrast, our model introduces tunable parameters ϵ_{b} and ϵ_{ss} that allow for accurate reproduction of experimental densities without compromising the prediction of phase boundaries. The observed density reduction is physically attributed to the increased population of solvent-mediated contacts relative to direct contacts. This mechanism introduces water-mediated porosity into the droplet and mimics the realistic hydration properties of protein condensates, thereby offering a more physically realistic description of IDP phase separation.

Discussions and Conclusion

Coarse-grained molecular simulations have become indispensable for elucidating the molecular principles underlying LLPS, complementing both theoretical frameworks and experimental observations. While residue-level models with implicit solvent have achieved remarkable success in capturing sequence-dependent phase behaviors of biomolecules, they often face a fundamental tradeoff due to the neglect of explicit solvent excluded volume and hydration effects. Specifically, interaction parameters calibrated to match single-chain dimensions or critical temperatures frequently result in an overestimation of the condensed phase density. This limitation suggests that standard Lennard-Jones potentials, which couple phase stability and density through a single energetic parameter, may lack the physical dimensionality required to fully describe the thermodynamics of hydrated protein condensates.

To address this challenge, we developed a coarse-grained framework that explicitly incorporates desolvation effects into the pairwise energy function. Application of this model to homopolymer systems demonstrates that desolvation substantially reshapes phase behavior. Incorporating desolvation modulates the critical temperature and alters the phase diagram by regulating intermolecular packing within the dense phase. Moreover, the model reveals a tight coupling between desolvation-controlled chain compaction during the formation of condensate phase and the thermal distance from criticality (temperature gap), providing a theoretical basis for linking single-chain conformational changes (ΔR_g) to macroscopic phase behavior. Dynamic analysis further captures the three characteristic stages of the early stage of LLPS, including spinodal decomposition, kinetic arrest, and coarsening. Crucially, it reveals how desolvation effect regulates the kinetics of these stages by modulating the effective inter-chain interactions and the roughness of the energy landscape. These results underscore the importance of accounting for desolvation energetics in governing both the thermodynamics and kinetics of LLPS.

Parameters	HPS model	CALVADOS2 model
α_{b}	0.33	0.30
α_{ss}	0.06	0.03
ϵ (kcal/mol)	0.20	0.262

Table 1. Desolvation parameters α_b and α_{ss} derived by fitting all-atom MD simulations.

The optimized parameter ϵ for CALVADOS2 is also listed together with that used in the HPS model.

Motivated by these insights, we further developed a transferable parameterization strategy for residue-level models. The resulting desolvation-aware CG model improves the accuracy of IDP conformational ensembles and LLPS thermodynamics while preserving the computational efficiency inherent to CG methodologies. By bridging the gap between the computational efficiency of implicit-solvent representations and the physicochemical realism of water-mediated interactions, this framework provides a mechanistic means to decouple the control of phase stability (T_c) from the regulation of condensed-phase density (ρ_{dense}). This decoupling effectively mitigates the over-compaction of dense phase commonly observed in implicit solvent simulations with CG models, enabling the molecular simulations qualitatively more consistent with the physical nature of biological condensates.

Despite these advances, the current model employs a single set of desolvation parameters (α_{b}, α_{ss}) for all amino acid types. While this simplification is effective for capturing global phase behavior, it overlooks residue-specific desolvation energetics that may influence selective interactions in heterogeneous or compositionally complex sequences. Future extensions of the model could incorporate residue-specific desolvation parameters derived from bottom-up parameterization or expanded experimental datasets, thereby enhancing predictive accuracy for sequence-dependent LLPS.

In summary, this work introduces a versatile and transferable extension to existing coarsegrained force fields that explicitly incorporates the physics of water-mediated interactions. By enabling efficient and realistic treatment of desolvation, the model provides a robust framework for simulating biomolecular condensates with improved thermodynamic and structural fidelity, as well as more accurate kinetic characterization. Future developments, such as residue-specific desolvation energetics and extensions to multicomponent systems involving nucleic acids, hold strong potential for deepening our mechanistic understanding of the complex phase behaviors that organize cellular biochemistry.

Methods

All-atom MD simulations

The all-atom MD simulations were performed using GROMACS. Ten amino acid analogues were solvated in a cubic water box under periodic boundary conditions. The OPLS-AA force field was used to model the solute molecules, and the TIP4P water model was employed to represent solvent. Na^+ and Cl^- ions were added to neutralize the system, yielding a total system size of 1,010 atoms. After an initial energy minimization of 5×10^4 steps, the system was equilibrated in the NVT ensemble at 298 K for 100 ps, followed by an NPT equilibration at 298 K and 1 atm for 1 ns. Temperature and pressure were controlled using the Nosé–Hoover thermostat and Parrinello–Rahman barostat Parrinello and Rahman (1981), respectively. A time step of 2 fs was used for all MD steps. The simulation details are provided in Table 2. Subsequently, a production simulation of 100 ns was performed under the same NPT conditions for structural and thermodynamic analysis. The intermolecular separation r between two amino acid analogues was defined as the distance between their C atoms. The potential of mean force (PMF) was computed as $\mathrm{PMF}(r) = -k_{\mathrm{B}}T \ln P(r)$, where $P(r)$ is the probability distribution of intermolecular distances obtained from the production trajectory.

Coarse-grained simulations

We utilized the slab method Dignon et al. (2018b) to extract the densities of the coexisting dilute and dense phases. In these simulations, 100 protein chains were placed in a rectangular box of dimensions 15 nm × 15 nm × 280 nm. The density profile along the z-axis was computed to identify the condensed and dilute regions, from which thermodynamic quantities such as the critical temperature were subsequently determined. Simulations were performed over a range of different temperatures. To implement the pairwise interaction potentials of the HPS model, we employed the azplugins package (*https://github.com/mphowardlab/azplugins*) together with HOOMD-blue v2.9.7 Anderson et al. (2020), running with GPU acceleration. All simulations used

Parameter	Value / Method	Description
Software	GROMACS	Version 2021.3
Force Field	OPLS-AA	-
Simulation Time	100 ns	5×10^7 steps
Integration Step (Δt)	2 fs	-
Integrator	Leap-frog	Standard MD algorithm
Temperature Coupling		
Temperature (T)	298.15 K	Reference temperature
Thermostat	Nose-Hoover	$\tau_T = 2.0$ ps
Pressure Coupling		
Pressure (P)	1.0 bar	Reference pressure
Barostat	Parrinello-Rahman	$\tau_P = 4.0$ ps
Compressibility (κ)	4.46×10^{-5} bar^{-1}	-
Non-bonded Interactions		
Electrostatics	PME	Particle Mesh Ewald
Coulomb Cut-off (r_{elec})	1.0 nm	-
vdW Cut-off (r_{vdw})	1.0 nm	-
Dispersion Correction	EnerPres	For energy and pressure
Constraints		
Algorithm	LINCS	Linear Constraint Solver
Constraints	h-bonds	Bonds involving H atoms

Table 2. **Summary of the production run parameters for all-atom molecular dynamics simulations.**

a time step of 0.01 ps. Each trajectory was first equilibrated for 3×10^7 steps, followed by a production run of 1×10^8 steps. Additional details of the simulation framework are provided in Table 3.

Hydrophobicity Scale Model

Our desolvation model is developed based on the hydrophobicity scale (HPS) coarse-grained model by Dignon et al. (2018b), in which each residue is represented by a single bead. The potential energy includes bonded term, electrostatic term and short-range pairwise term. The bonded interaction term is given by a harmonic potential $V^b = k_b(r_{i,i+1} - r^0)^2$ with the spring constant k_b = 10 kJ/Å^2 and the bonded length r^0 = 0.38 Å. $r_{i,i+1}$ represents the distance between the consecutive residues i and $i + 1$ along the protein chain. The electrostatic interaction term is modeled by a Coulombic potential with Debye-Hückel Debye and Hückel (1923) electrostatic screening caused by salt ion concentration. The function is given by

$$V_{ij}^{ele}(r) = \frac{q_i q_j}{4\pi D r}\exp(-r/\kappa), \tag{3}$$

where κ is the screening length and D = 80, which is the relative dielectric constant of water. For the short-range pairwise interaction, the HPS model uses a 6-12 Lennard-Jones potential with the interaction strength given by hydrophobicity scale Kapcha and Rossky (2014), which can describe the effective interaction between residues. The hydrophobicity value λ, ranging from 0 to 1, varies for different residues. The arithmetic average is used for the interaction parameter between two residues, i.e. hydrophobicity value $\lambda_{i,j} = (\lambda_i + \lambda_j)/2$ and amino acid size $\sigma_{i,j} = (\sigma_i + \sigma_j)/2$. The energy function of the short-range pairwise interaction is given by

$$\Phi(r) = \begin{cases} \Phi_{LJ} + (1-\lambda)\epsilon, & \text{if } r \leqslant 2^{1/6}\sigma \\ \lambda\Phi_{LJ}, & \text{otherwise} \end{cases} \tag{4}$$

where Φ_{LJ} is standard 6-12 Lennard-Jones potential

$$\Phi_{LJ} = 4\epsilon\left[\left(\frac{\sigma}{r}\right)^{12} - \left(\frac{\sigma}{r}\right)^{6}\right]. \tag{5}$$

The free parameter ϵ is set as 0.2 kcal/mol, with which the molecular simulations can best reproduce the experimental results of R_g values for a set of IDPs.

Simulation Framework

We use slab simulation scheme in the coexistence simulations. Initially, 100 chains are randomly distributed in a cubic box with periodic boundary condition at 200 K. The box length is first scaled to 15 nm, which can effectively prevent protein chains from interacting with their periodic images generated by periodic boundary conditions. Then, the x- and y-dimensions are set fixed and the z-dimension is extended to 280 nm. The temperature is then gradually increased to the target temperature and the simulations are conducted at different temperatures for 1 μs in the NVT ensemble maintained by a Langevin thermostat, with a friction coefficient of 0.01 ps^{-1}. A time step of 0.01 ps is used for all the simulations. We use HOOMD-Blue v2.9.7 packages Anderson et al. (2020) to conduct the simulations, which utilizes both CPU and GPU resources to accelerate calculation.

The slab density profile along z-axis is then determined after the system gets equilibrated. In order to avoid the influence of periodic boundary conditions, we first move the center of mass of the system in the z-axis direction to the position of z = 0. We then determined the distribution of dense phase and dilute phase of the phase separated system using the defined thresholds. The area with density higher than 0.95 of the maximum density ($\rho_{\max}$) is treated as dense phase, and their

Parameter	Value / Method	Description
General Settings		
Software	HOOMD-blue	v2.9.7 with azplugins
Integrator	Langevin	Stochastic dynamics
Time Step (Δt)	0.01 ps	-
Total Simulation Time	1 μs	10^8 steps
Temperature (T)	Variable	See main text
Friction Coefficient (γ)	$m_i/1000$ ps^{-1}	Mass-dependent
System Geometry		
Box Dimensions (x, y)	15.0 nm	Periodic boundaries
Box Dimension (z)	280.0 nm	Slab configuration
Interactions		
Bond Potential	Harmonic	$k = 8368$ kJ·mol^{-1}nm^{-2}, $r_0 = 0.38$ nm
Non-bonded Potential	Ashbaugh-Hatch	HPS model (via azplugins)
Electrostatics	Yukawa	Screened Coulomb potential
Screening Constant (κ)	1.0 nm^{-1}	Inverse Debye length
Coulomb Cut-off	3.5 nm	-
Neighbor List	Cell List	Exclusions: 1-2, body

Table 3. Summary of the coarse-grained molecular dynamics simulation parameters used in the slab simulations.

average density is regarded as the phase density of the dense phase (ρ_{dense}). For the dilute phase, the threshold is taken as ρ_{min} + 50 mg/mL, where ρ_{min} is the minimum density. The density of dilute phase (ρ_{dilute}) is then determined by the same method. If $\rho_{max} - \rho_{min} < 50$ mg/mL, the system is considered not to undergo phase separation.

Critical Temperature

The critical temperature was determined based on the vapor-liquid interfacial properties of Lennard-Jones chains Blas et al. (2008). The critical temperature T_c is obtained from ρ_{dense} and ρ_{dilute} at different temperatures by

$$\rho_{\text{dense}} - \rho_{\text{dilute}} = A(T_c - T)^{\beta}, \tag{6}$$

where β is the critical exponent, which is set as 0.325 Rowlinson and Widom (2013) and A is the fitting parameter. Data with temperature below the critical temperature is used to fit this equation. The phase density at critical temperature is determined by the law of rectilinear diameters Davies (1912)

$$\frac{\rho_{\text{dense}} + \rho_{\text{dilute}}}{2} = B + C \cdot T, \tag{7}$$

with B and C being the free parameters determined from the simulation data. At the critical temperature, the distinction between dense phase and dilute phase disappears, which means $\rho_{dense} = \rho_{dilute} = \rho_c$. The phase density is then calculated by $\rho_c = B + C \cdot T_c$. A phase diagram which shows temperature change with the density of dense phase and dilute phase is then obtained.

Derivation of the Reduced Diffusion Coefficient

To investigate the intrinsic influence of the interaction potential on chain dynamics, we must isolate the structural contributions from the trivial thermal acceleration. While keeping the quench depth (T/T_c) constant ensures thermodynamic consistency, it necessitates varying the absolute temperature T, which inherently alters the base diffusion rate via thermal fluctuations. To resolve this, we adopt the constant quench depth approach to ensure thermodynamic consistency and introduce a normalized metric to eliminate the trivial thermal velocity contribution.

According to the fundamental Einstein relation, which connects the diffusion coefficient K to the thermal energy k_BT and the friction coefficient ζ:

$$K(T) = \frac{k_B T}{\zeta(T,\phi,\epsilon)} \tag{8}$$

Here, the friction coefficient ζ encapsulates all resistance to motion. Following the hybrid theoretical framework proposed by Macedo and Litovitz Macedo and Litovitz (1965), which unifies free-volume theory with activated rate theory, the friction term can be factorized into a packing-dependent contribution and an energy-barrier-dependent contribution:

$$\zeta(T,\phi,\epsilon) \propto \exp\left(\frac{\gamma v^*}{v_f(\phi)}\right) \times \exp\left(\frac{E_{\text{eff}}(\epsilon)}{k_B T}\right) \tag{9}$$

where the first term represents the hindrance due to limited free volume (v_f), governed by the packing density Φ, and the second term is the Arrhenius factor describing the activated hopping over an effective energy barrier E_{eff}, which corresponds to the roughness of the energy landscape induced by the desolvation potential.

In our analysis, by fixing the quench depth (T/T_c), we ensure that the macroscopic packing density Φ remains comparable across different systems (as verified by the phase diagram in main text). Consequently, the free-volume contribution to friction is effectively invariant. Substituting this

back into Equation (8), the diffusion coefficient scales as:

$$K(T) \sim T \cdot \exp\left(-\frac{E_{\text{eff}}(\epsilon)}{k_{\text{B}}T}\right) \tag{10}$$

The pre-factor T represents the trivial thermal acceleration inherent to Brownian motion. To isolate the intrinsic energy landscape signature, we define the reduced diffusion coefficient $\tilde{K}$ by normalizing out this linear thermal contribution:

$$\tilde{K} \equiv \frac{K}{T} \propto \exp\left(-\frac{E_{\text{eff}}(\epsilon)}{k_{\text{B}}T}\right) \tag{11}$$

Thus,$\tilde{K}$ serves as a physically rigorous metric to isolate the intrinsic influence of the energy function on chain dynamics. By normalizing out the trivial linear thermal velocity contribution inherent to Brownian motion, this definition is necessary to decouple the specific kinetic modulation imposed by the desolvation potential from the background thermal acceleration and thermodynamic driving forces. Consequently, $\tilde{K}$ allows for a direct assessment of how the interaction potential fundamentally alters transport properties, independent of the trivial temperature effects required to maintain thermodynamic consistency.

Calculation of Normalized Density Variance

To quantify the rate of density fluctuation growth during the early stage of phase separation, we first computed the instantaneous spatial variance of the density profile along the *z*-axis, $\sigma_\rho^2(t)$, defined as

$$\sigma_\rho^2(t) = \frac{1}{L_z}\int_0^{L_z} [\rho(z,t) - \bar{\rho}]^2 \, \mathrm{d}z \tag{12}$$

where $\rho(z, t)$ is the local density at position z and time t, and $\bar{\rho}$ is the mean density of the system. To enable a fair comparison of kinetics across systems with distinct interaction parameters (ϵ_{ss} and ϵ_{b}), it is crucial to decouple the rate of phase separation from the difference in equilibrium densephase densities. Therefore, we normalized the instantaneous variance by its equilibrium baseline:

$$\hat{\sigma}_\rho^2(t) = \frac{\sigma_\rho^2(t)}{\langle \sigma_\rho^2 \rangle_{\text{eq}}}. \tag{13}$$

Here, the normalization factor $\langle \sigma_\rho^2 \rangle_{\text{eq}}$ is the time-averaged density variance calculated from the final 30% of the simulation process. This period corresponds to the steady state characterized by the formation of a well-defined slab with stabilized phase densities. By using this normalized metric $\hat{\sigma}_\rho^2(t)$, we effectively factor out the variations in final density contrast, ensuring that the observed differences in the time-evolution curves purely reflect the acceleration or deceleration of the kinetic process itself.

Desolvation Parameters

Due to the lack of experimental data, the empirical parameters α_{b} and α_{ss} were estimated using all-atom molecular dynamics simulations of amino acid analogues with explicit solvent. The potential of mean force (PMF) obtained from the simulation results is shown in Figure 1—figure supplement 1. Methane (CH_4), methanol (CH_3OH), acetate ion $(C_2H_3O_2^-)$, ammonium ion (NH_4^+), and methanamide (CH_3NO) were chosen as representative amino acid analogues for non-polar, polar, negatively charged, positively charged, and backbone-like residues, respectively. The α_{b}, α_{ss} values were then obtained by fitting the nonbonded energy function with desolvation effect

(Equation (1)) to the experimental PMF results. The λ parameter values for these amino acid analogous were assigned based on the λ values of the corresponding amino acids. Specifically, we used λ_{GLY} = 0.649 for methane, λ_{SER} = 0.595 for methanol and λ_{CYS} = 0.595 for methanamide. The results are shown in Table 1.

Data availability

All simulation codes, input files, and scripts for plotting figures of the manuscript are openly available on GitHub at *https://github.com/kaizhangnju/desolvation-CG-model*. Additional data supporting the findings of this work are available from the corresponding author upon reasonable request due to large file size constraints.

Figure supplements

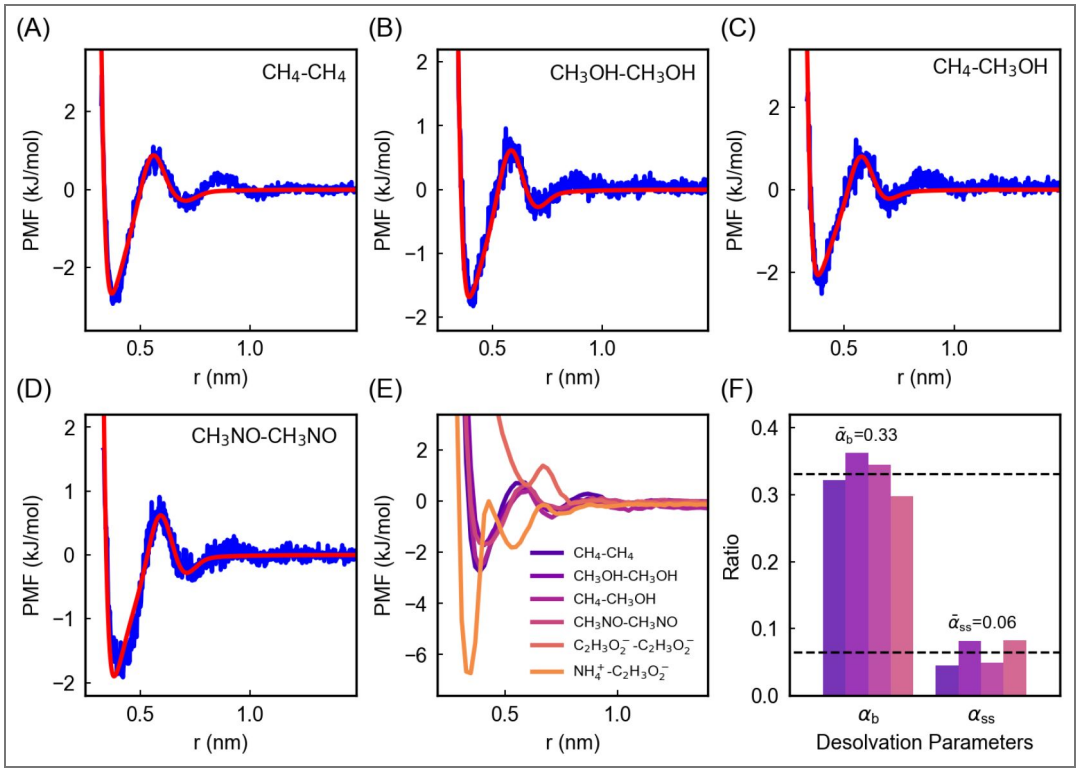

Figure 1—figure supplement 1. Desolvation effect from all-atom MD simulations. (A-D) PMFs from all-atom simulations and the fitting with desolvation energy function (Eq. 1) for different pairs of amino acid analogues at physiological salt concentration. (E) The collection of the fitted PMFs for different pairs of amino acid analogues. (F) The extracted α_b and α_{ss} values for different pairs of amino acid analogues.

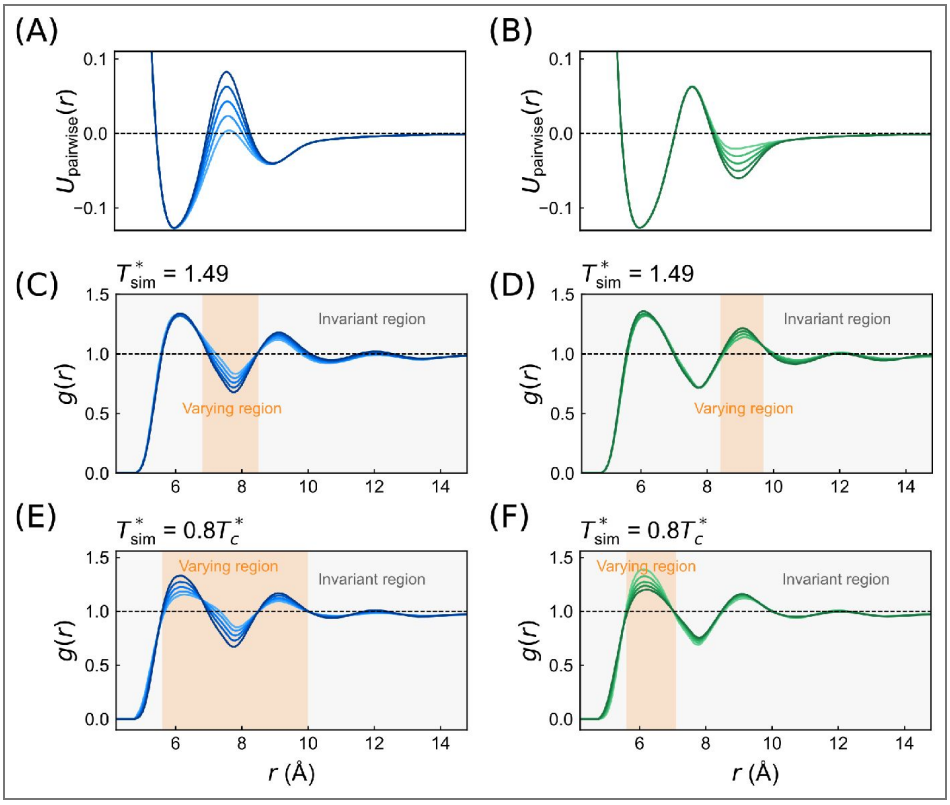

Figure 2—figure supplement 1. Effect of desolvation on the radial distribution of the residue pairs of the homopolymer chains.

(A, B) Schematic figures for the change of desolvation potential. (C, D) The radial distribution functions between inter-chain and intra-chain residue pairs for simulations with different ϵ_b and different ϵ_{ss} at the same temperature (T^* = 1.49). (E, F) The radial distribution functions between all residue pairs in the dense phase for simulations with different ϵ_b and different ϵ_{ss} at the same temperature ($T^* = 0.8T_c^*$)

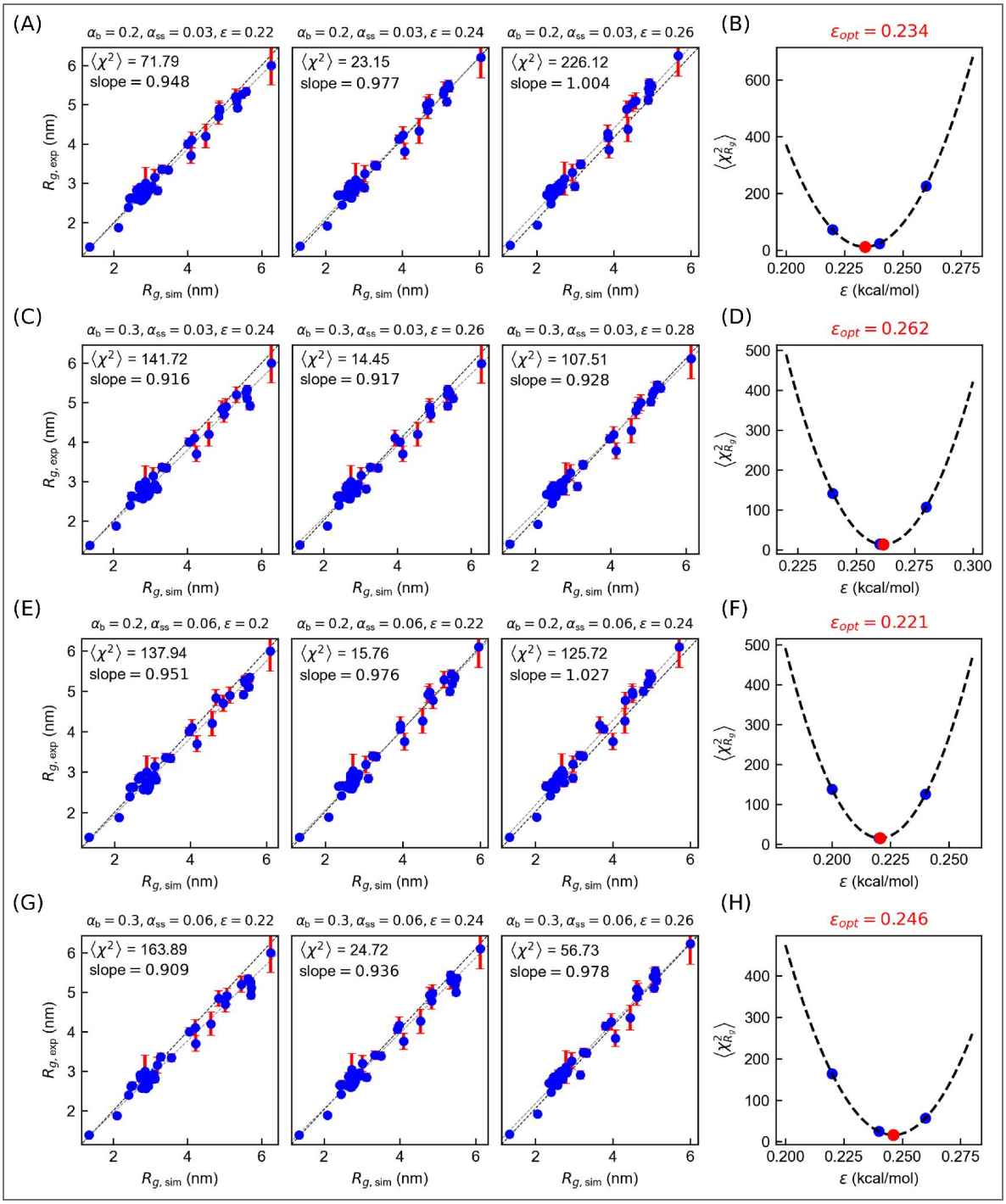

Figure 5—figure supplement 1. Optimizing the desolvation parameters for the CALVADOS2 model by using experimental R_g data.

(A,C,E,G) Correlation between experimental R_g values and simulation R_g values with different desolvation parameters. (B,D,F,H) $\left\langle\chi^2_{R_g}\right\rangle$ values as a function of for different sets of desolvation parameters. The optimal ϵ values are also shown.

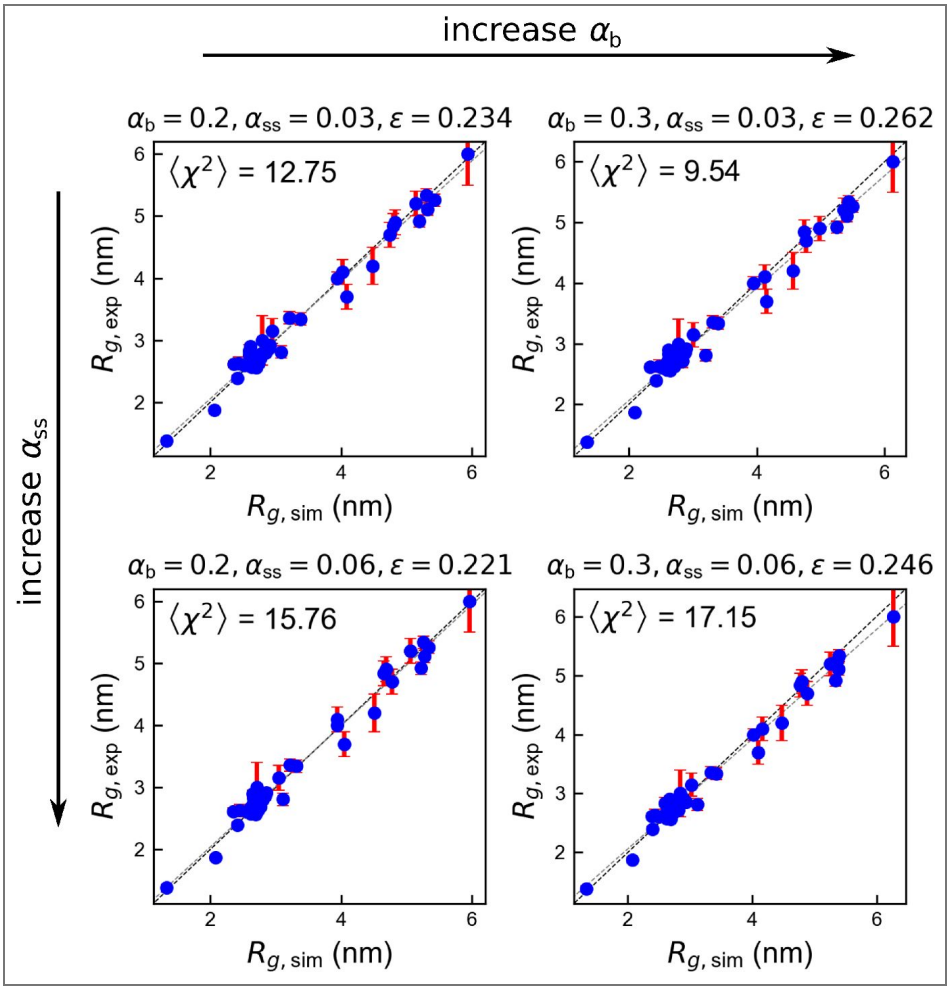

Figure 5—figure supplement 2. **Correlation between experimental R_g values and simulation R_g values with different α_b and α_{ss} values and the corresponding optimized ϵ values for the CALVADOS2 model.**

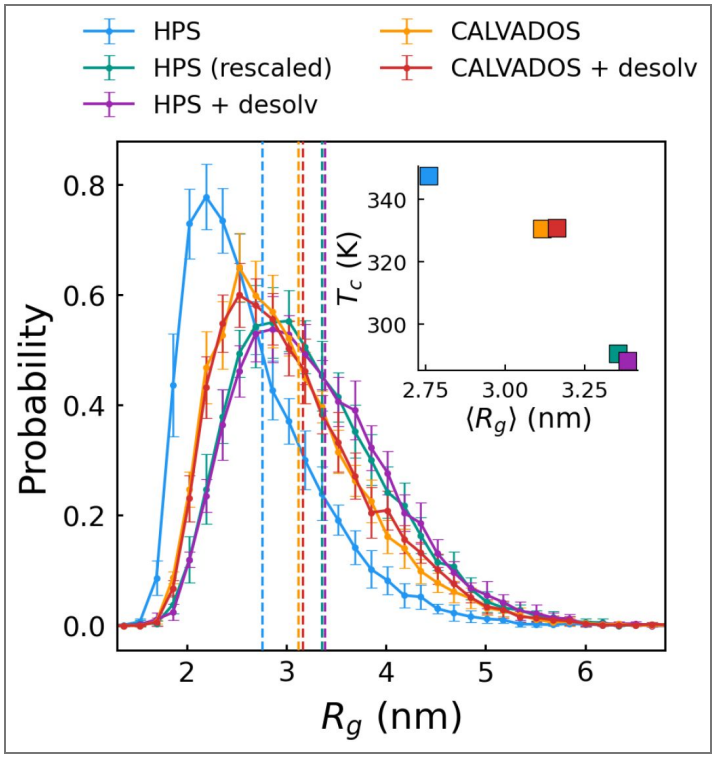

Figure 5—figure supplement 3. **Comparison of single chain radius of gyration (R_g) for HPS model, HPS + desolvation, HPS (ϵ rescaled to 0.16 kcal/mol), CALVADOS2 model and CALVADOS + desolvation.**

Additional information

Author ORCID iDs

Kai Zhang: https://orcid.org/0009-0002-1486-7206

References

Anderson JA, Glaser J, Glotzer SC (2020) HOOMD-blue: A Python package for high-performance molecular dynamics and hard particle Monte Carlo simulations. *Computational Materials Science* **173**:109363 https://doi.org/10.1016/j.commatsci.2019.109363

Aspromonte MC, Nugnes MV, Quaglia F, Bouharoua A, Tosatto SC, Piovesan D. (2024) DisProt in 2024: improving function annotation of intrinsically disordered proteins. *Nucleic Acids Research* **52**:D434-D441 https://doi.org/10.1093/nar/gkad928 | PubMed

Baul U, Chakraborty D, Mugnai ML, Straub JE, Thirumalai D. (2019) Sequence effects on size, shape, and structural heterogeneity in intrinsically disordered proteins. *The Journal of Physical Chemistry B* **123**:3462-3474 https://doi.org/10.1021/acs.jpcb.9b02575 | PubMed

Benayad Z, von Bulow S, Stelzl LS, Hummer G. (2020) Simulation of FUS protein condensates with an adapted coarse-grained model. *Journal of chemical theory and computation* **17**:525-537 https://doi.org/10.1021/acs.jctc.0c01064

Biamonti G, Vourc'h C. (2010) Nuclear stress bodies. *Cold Spring Harbor perspectives in biology* **2**:a000695 https://doi.org/10.1101/cshperspect.a000695 | PubMed

Bian Y, Lv F, Pan H, Ren W, Zhang W, Wang Y, Cao Y, Li W, Wang W. (2024) Fusion Dynamics and Size-Dependence of Droplet Microstructure in ssDNA-Mediated Protein Phase Separation. *JACS Au* **4**:3690-3704 https://doi.org/10.1021/jacsau.4c00690 | PubMed

Blas FJ, MacDowell LG, de Miguel E, Jackson G. (2008) Vapor-liquid interfacial properties of fully flexible Lennard-Jones chains. *The Journal of chemical physics* **129** https://doi.org/10.1063/1.2989115 | PubMed

Boeynaems S, Alberti S, Fawzi NL, Mittag T, Polymenidou M, Rousseau F, Schymkowitz J, Shorter J, Wolozin B, Van Den Bosch L, *et al.* (2018) Protein phase separation: a new phase in cell biology. *Trends in cell biology* **28**:420-435 https://doi.org/10.1016/j.tcb.2018.02.004 | PubMed

Burke KA, Janke AM, Rhine CL, Fawzi NL (2015) Residue-by-residue view of in vitro FUS granules that bind the C-terminal domain of RNA polymerase II. *Molecular cell* **60**:231-241 https://doi.org/10.1016/j.molcel.2015.09.006 | PubMed

Cahn JW (1961) On spinodal decomposition. *Acta metallurgica* **9**:795-801 https://doi.org/10.1016/0001-6160(61)90182-1

Cahn JW, Hilliard JE (1958) Free energy of a nonuniform system. I. Interfacial free energy. *The Journal of chemical physics* **28**:258-267 https://doi.org/10.1063/1.1744102

Camilloni C, Bonetti D, Morrone A, Giri R, Dobson CM, Brunori M, Gianni S, Vendruscolo M. (2016) Towards a structural biology of the hydrophobic effect in protein folding. *Scientific reports* **6**:28285 https://doi.org/10.1038/srep28285 | PubMed

Chen T, Chan HS (2014) Effects of desolvation barriers and sidechains on local–nonlocal coupling and chevron behaviors in coarse-grained models of protein folding. *Physical Chemistry Chemical Physics* **16**:6460-6479 https://doi.org/10.1039/c3cp54866j | PubMed

Cheung MS, García AE, Onuchic JN (2002) Protein folding mediated by solvation: water expulsion and formation of the hydrophobic core occur after the structural collapse. *Proceedings of the National Academy of Sciences* **99**:685-690 https://doi.org/10.1073/pnas.022387699 | PubMed

Choi JM, Dar F, Pappu RV (2019) LASSI: A lattice model for simulating phase transitions of multivalent proteins. *PLoS computational biology* **15**:e1007028 https://doi.org/10.1371/journal.pcbi.1007028 | PubMed

Conicella AE, Zerze GH, Mittal J, Fawzi NL (2016) ALS mutations disrupt phase separation mediated by α-helical structure in the TDP-43 low-complexity C-terminal domain. *Structure* **24**:1537-1549 https://doi.org/10.1016/j.str.2016.07.007 | PubMed

Dannenhoffer-Lafage T, Best RB (2021) A data-driven hydrophobicity scale for predicting liquid–liquid phase separation of proteins. *The Journal of Physical Chemistry B* **125**:4046-4056 https://doi.org/10.1021/acs.jpcb.0c11479 | PubMed

Darré L, Machado MR, Brandner AF, González HC, Ferreira S, Pantano S. (2015) SIRAH: a structurally unbiased coarsegrained force field for proteins with aqueous solvation and long-range electrostatics. *Journal of chemical theory and computation* **11**:723-739 https://doi.org/10.1021/ct5007746

Davies H. (1912) XXXVI. On some applications of the law of the rectilinear diameter. *The London, Edinburgh, and Dublin Philosophical Magazine and Journal of Science* **24**:415-424 https://doi.org/10.1080/14786440908637343

Davtyan A, Schafer NP, Zheng W, Clementi C, Wolynes PG, Papoian GA (2012) AWSEM-MD: protein structure prediction using coarse-grained physical potentials and bioinformatically based local structure biasing. *The Journal of Physical Chemistry B* **116**:8494-8503 https://doi.org/10.1021/jp212541y | PubMed

De Jong DH, Singh G, Bennett WD, Arnarez C, Wassenaar TA, Schafer LV, Periole X, Tieleman DP, Marrink SJ (2013) Improved parameters for the martini coarse-grained protein force field. *Journal of chemical theory and computation* **9**:687-697 https://doi.org/10.1021/ct300646g | PubMed

Debye P, Hückel E. (1923) De la theorie des electrolytes. I. abaissement du point de congelation et phenomenes associes. *Physikalische Zeitschrift* **24**:185-206

Dignon GL, Best RB, Mittal J. (2020) Biomolecular phase separation: from molecular driving forces to macroscopic properties. *Annual review of physical chemistry* **71**:53-75 https://doi.org/10.1146/annurev-physchem-071819-113553 | PubMed

Dignon GL, Zheng W, Best RB, Kim YC, Mittal J. (2018) Relation between single-molecule properties and phase behavior of intrinsically disordered proteins. *Proceedings of the National Academy of Sciences* **115**:9929-9934 https://doi.org/10.1073/pnas.1804177115 | PubMed

Dignon GL, Zheng W, Kim YC, Best RB, Mittal J. (2018) Sequence determinants of protein phase behavior from a coarse-grained model. *PLoS computational biology* **14**:e1005941 https://doi.org/10.1371/journal.pcbi.1005941 | PubMed

Doi M, Edwards SF, Edwards SF (1988) *The theory of polymer dynamics* **73** oxford university press.

Elbaum-Garfinkle S, Kim Y, Szczepaniak K, Chen CCH, Eckmann CR, Myong S, Brangwynne CP (2015) The disordered P granule protein LAF-1 drives phase separation into droplets with tunable viscosity and dynamics. *Proceedings of the National Academy of Sciences* **112**:7189-7194 https://doi.org/10.1073/pnas.1504822112 | PubMed

Espinosa JR, Joseph JA, Sanchez-Burgos I, Garaizar A, Frenkel D, Collepardo-Guevara R. (2020) Liquid network connectivity regulates the stability and composition of biomolecular condensates with many components. *Proceedings of the National Academy of Sciences* **117**:13238-13247 https://doi.org/10.1073/pnas.1917569117 | PubMed

Ferguson A, Liu Z, Chan HS (2009) Desolvation barrier effects are a likely contributor to the remarkable diversity in the folding rates of small proteins. *Journal of molecular biology* **389**:619-636 https://doi.org/10.1016/j.jmb.2009.04.011 | PubMed

Feric M, Vaidya N, Harmon TS, Mitrea DM, Zhu L, Richardson TM, Kriwacki RW, Pappu RV, Brangwynne CP (2016) Coexisting liquid phases underlie nucleolar subcompartments. *Cell* **165**:1686-1697 https://doi.org/10.1016/j.cell.2016.04.047 | PubMed

Flory PJ (1942) Thermodynamics of high polymer solutions. *The Journal of chemical physics* **10**:51-61 https://doi.org/10.1063/1.1723621

Flory PJ (1953) *Principles of polymer chemistry* Cornell university press.

Gasic AG, Cheung MS (2020) A tale of two desolvation potentials: An investigation of protein behavior under high hydrostatic pressure. *The Journal of Physical Chemistry B* **124**:1619-1627 https://doi.org/10.1021/acs.jpcb.9b10734 | PubMed

Harmon TS, Holehouse AS, Rosen MK, Pappu RV (2017) Intrinsically disordered linkers determine the interplay between phase separation and gelation in multivalent proteins. *eLife* **6**:e30294 https://doi.org/10.7554/eLife.30294 | PubMed

Hazra MK, Levy Y. (2021) Biophysics of phase separation of disordered proteins is governed by balance between short-and long-range interactions. *The Journal of Physical Chemistry B* **125**:2202-2211 https://doi.org/10.1021/acs.jpcb.0c09975 | PubMed

Hnisz D, Shrinivas K, Young RA, Chakraborty AK, Sharp PA (2017) A phase separation model for transcriptional control. *Cell* **169**:13-23 https://doi.org/10.1016/j.cell.2017.02.007 | PubMed

Huggins ML (1941) Solutions of long chain compounds. *The Journal of chemical physics* **9**:440-440 https://doi.org/10.1063/1.1750930

Huggins ML (1942) Some properties of solutions of long-chain compounds. *The Journal of Physical Chemistry* **46**:151-158 https://doi.org/10.1021/j150415a018

Joseph JA, Reinhardt A, Aguirre A, Chew PY, Russell KO, Espinosa JR, Garaizar A, Collepardo-Guevara R. (2021) Physicsdriven coarse-grained model for biomolecular phase separation with near-quantitative accuracy. *Nature Computational Science* **1**:732-743 https://doi.org/10.1038/s43588-021-00155-3 | PubMed

Jussupow A, Bartley D, Lapidus LJ, Feig M. (2025) COCOMO2: A coarse-grained model for interacting folded and disordered proteins. *Journal of Chemical Theory and Computation* **21**:2095-2107 https://doi.org/10.1021/acs.jctc.4c01460 | PubMed

Kapcha LH, Rossky PJ (2014) A simple atomic-level hydrophobicity scale reveals protein interfacial structure. *Journal of molecular biology* **426**:484-498 https://doi.org/10.1016/j.jmb.2013.09.039 | PubMed

Karanicolas J, Brooks III CL (2002) The origins of asymmetry in the folding transition states of protein L and protein G. *Protein Science* **11**:2351-2361 https://doi.org/10.1110/ps.0205402 | PubMed

Latham AP, Zhang B. (2019) Maximum entropy optimized force field for intrinsically disordered proteins. *Journal of chemical theory and computation* **16**:773-781 https://doi.org/10.1021/acs.jctc.9b00932 | PubMed

Latham AP, Zhang B. (2021) Consistent force field captures homologue-resolved HP1 phase separation. *Journal of chemical theory and computation* **17**:3134-3144 https://doi.org/10.1021/acs.jctc.0c01220 | PubMed

Li L, Hou Z. (2023) Crosslink-induced conformation change of intrinsically disordered proteins have a nontrivial effect on phase separation dynamics and thermodynamics. *The Journal of Physical Chemistry B* **127**:5018-5026 https://doi.org/10.1021/acs.jpcb.3c01728 | PubMed

Li W, Wang W, Takada S. (2014) Energy landscape views for interplays among folding, binding, and allostery of calmodulin domains. *Proceedings of the National Academy of Sciences* **111**:10550-10555 https://doi.org/10.1073/pnas.1402768111 | PubMed

Lin YH, Chan HS (2017) Phase separation and single-chain compactness of charged disordered proteins are strongly correlated. *Biophysical Journal* **112**:2043-2046 https://doi.org/10.1016/j.bpj.2017.04.021 | PubMed

Lin YH, Song J, Forman-Kay JD, Chan HS (2017) Random-phase-approximation theory for sequence-dependent, biologically functional liquid-liquid phase separation of intrinsically disordered proteins. *Journal of Molecular Liquids* **228**:176-193 https://doi.org/10.1016/j.molliq.2016.09.090

Liu Z, Chan HS (2005) Solvation and desolvation effects in protein folding: native flexibility, kinetic cooperativity and enthalpic barriers under isostability conditions. *Physical biology* **2**:S75 https://doi.org/10.1088/1478-3975/2/4/s01 | PubMed

Macedo P, Litovitz T. (1965) On the relative roles of free volume and activation energy in the viscosity of liquids. *The Journal of Chemical Physics* **42**:245-256 https://doi.org/10.1063/1.1695683

Majumdar SN, Huse DA, Lubachevsky BD (1994) Growth of long-range correlations after a quench in conserved-order-parameter systems. *Physical review letters* **73**:182 https://doi.org/10.1103/physrevlett.73.182 | PubMed

McCarty J, Delaney KT, Danielsen SP, Fredrickson GH, Shea JE (2019) Complete phase diagram for liquid–liquid phase separation of intrinsically disordered proteins. *The journal of physical chemistry letters* **10**:1644-1652 https://doi.org/10.1021/acs.jpclett.9b00099 | PubMed

Metzler R, Jeon JH, Cherstvy AG, Barkai E. (2014) Anomalous diffusion models and their properties: non-stationarity, non-ergodicity, and ageing at the centenary of single particle tracking. *Physical Chemistry Chemical Physics* **16**:24128-24164 https://doi.org/10.1039/c4cp03465a | PubMed

Molliex A, Temirov J, Lee J, Coughlin M, Kanagaraj AP, Kim HJ, Mittag T, Taylor JP (2015) Phase separation by low complexity domains promotes stress granule assembly and drives pathological fibrillization. *Cell* **163**:123-133 https://doi.org/10.1016/j.cell.2015.09.015 | PubMed

Morimoto M, Boerkoel CF (2013) The role of nuclear bodies in gene expression and disease. *Biology* **2**:976-1033 https://doi.org/10.3390/biology2030976 | PubMed

Mukherjee S, Ramos S, Pezzotti S, Kalarikkal A, Prass TM, Galazzo L, Gendreizig D, Barbosa N, Bordignon E, Havenith M, *et al.* (2024) Entropy tug-of-war determines solvent effects in the liquid–liquid phase separation of a globular protein. *The Journal of Physical Chemistry Letters* **15**:4047-4055 https://doi.org/10.1021/acs.jpclett.3c03421 | PubMed

Mukherjee S, Schäfer LV (2023) Thermodynamic forces from protein and water govern condensate formation of an intrinsically disordered protein domain. *Nature Communications* **14**:5892 https://doi.org/10.1038/s41467-023-41586-y | PubMed

Osterburg C, Dötsch V. (2022) Structural diversity of p63 and p73 isoforms. *Cell death & differentiation* **29**:921-937 https://doi.org/10.1038/s41418-022-00975-4 | PubMed

Parrinello M, Rahman A. (1981) Polymorphic transitions in single crystals: A new molecular dynamics method. *Journal of Applied physics* **52**:7182-7190 https://doi.org/10.1063/1.328693

Patel A, Lee HO, Jawerth L, Maharana S, Jahnel M, Hein MY, Stoynov S, Mahamid J, Saha S, Franzmann TM, *et al.* (2015) A liquid-to-solid phase transition of the ALS protein FUS accelerated by disease mutation. *Cell* **162**:1066-1077 https://doi.org/10.1016/j.cell.2015.07.047 | PubMed

Regy RM, Thompson J, Kim YC, Mittal J. (2021) Improved coarse-grained model for studying sequence dependent phase separation of disordered proteins. *Protein Science* **30**:1371-1379 https://doi.org/10.1002/pro.4094 | PubMed

Riback JA, Katanski CD, Kear-Scott JL, Pilipenko EV, Rojek AE, Sosnick TR, Drummond DA (2017) Stress-triggered phase separation is an adaptive, evolutionarily tuned response. *Cell* **168**:1028-1040 https://doi.org/10.1016/j.cell.2017.02.027 | PubMed

Rowlinson JS, Widom B. (2013) *Molecular theory of capillarity* Courier Corporation.

Ruff KM, Dar F, Pappu RV (2021) Ligand effects on phase separation of multivalent macromolecules. *Proceedings of the National Academy of Sciences* **118**:e2017184118 https://doi.org/10.1073/pnas.2017184118 | PubMed

Salari R, Chong LT (2012) Effects of high temperature on desolvation costs of salt bridges across protein binding interfaces: similarities and differences between implicit and explicit solvent models. *The Journal of Physical Chemistry B* **116**:2561-2567 https://doi.org/10.1021/jp210172b | PubMed

Shin Y, Brangwynne CP (2017) Liquid phase condensation in cell physiology and disease. *Science* **357**:eaaf4382 https://doi.org/10.1126/science.aaf4382 | PubMed

Souza PC, Alessandri R, Barnoud J, Thallmair S, Faustino I, Grünewald F, Patmanidis I, Abdizadeh H, Bruininks BM, Wassenaar TA, *et al.* (2021) Martini 3: a general purpose force field for coarse-grained molecular dynamics. *Nature methods* **18**:382-388 https://doi.org/10.1038/s41592-021-01098-3 | PubMed

Strom AR, Emelyanov AV, Mir M, Fyodorov DV, Darzacq X, Karpen GH (2017) Phase separation drives heterochromatin domain formation. *Nature* **547**:241-245 https://doi.org/10.1038/nature22989 | PubMed

Su X, Ditlev JA, Hui E, Xing W, Banjade S, Okrut J, King DS, Taunton J, Rosen MK, Vale RD (2016) Phase separation of signaling molecules promotes T cell receptor signal transduction. *Science* **352**:595-599 https://doi.org/10.1126/science.aad9964 | PubMed

Tanaka H. (2000) Viscoelastic phase separation. *Journal of Physics: Condensed Matter* **12**:R207 https://doi.org/10.1088/0953-8984/12/15/201

Tarus B, Straub JE, Thirumalai D. (2006) Dynamics of Asp23-Lys28 salt-bridge formation in Abeta10-35 monomers. *Journal of the American Chemical Society* **128**:16159-16168 https://doi.org/10.1021/ja064872y | PubMed

Tesei G, Lindorff-Larsen K. (2022) Improved predictions of phase behaviour of intrinsically disordered proteins by tuning the interaction range. *Open Research Europe* **2** https://doi.org/10.12688/openreseurope.14967.2 | PubMed

Tesei G, Schulze TK, Crehuet R, Lindorff-Larsen K. (2021) Accurate model of liquid–liquid phase behavior of intrinsically disordered proteins from optimization of single-chain properties. *Proceedings of the National Academy of Sciences* **118**:e2111696118 https://doi.org/10.1073/pnas.2111696118 | PubMed

Tesei G, Trolle AI, Jonsson N, Betz J, Knudsen FE, Pesce F, Johansson KE, Lindorff-Larsen K. (2024) Conformational ensembles of the human intrinsically disordered proteome. *Nature* **626**:897-904 https://doi.org/10.1038/s41586-023-07004-5 | PubMed

Uversky VN, Kuznetsova IM, Turoverov KK, Zaslavsky B. (2015) Intrinsically disordered proteins as crucial constituents of cellular aqueous two phase systems and coacervates. *FEBS letters* **589**:15-22 https://doi.org/10.1016/j.febslet.2014.11.028 | PubMed

Valdes-Garcia G, Heo L, Lapidus LJ, Feig M. (2023) Modeling concentration-dependent phase separation processes involving peptides and RNA via residue-based coarse-graining. *Journal of Chemical Theory and Computation* **19**:669-678 https://doi.org/10.1021/acs.jctc.2c00856 | PubMed

Van Der Lee R, Buljan M, Lang B, Weatheritt RJ, Daughdrill GW, Dunker AK, Fuxreiter M, Gough J, Gsponer J, Jones DT, *et al.* (2014) Classification of intrinsically disordered regions and proteins. *Chemical reviews* **114**:6589-6631 https://doi.org/10.1021/cr400525m | PubMed

Watanabe F, Akimoto T, Best RB, Lindorff-Larsen K, Metzler R, Yamamoto E. (2025) Diffusion of intrinsically disordered proteins within protein condensates. *Physical Review Research* **7**:043117 https://doi.org/10.1103/jsdl-chm9

Wei MT, Elbaum-Garfinkle S, Holehouse AS, Chen CCH, Feric M, Arnold CB, Priestley RD, Pappu RV, Brangwynne CP (2017) Phase behaviour of disordered proteins underlying low density and high permeability of liquid organelles. *Nature chemistry* **9**:1118-1125 https://doi.org/10.1038/nchem.2803 | PubMed

Wippich F, Bodenmiller B, Trajkovska MG, Wanka S, Aebersold R, Pelkmans L. (2013) Dual specificity kinase DYRK3 couples stress granule condensation/dissolution to mTORC1 signaling. *Cell* **152**:791-805 https://doi.org/10.1016/j.cell.2013.01.033 | PubMed

Wu H, Wolynes PG, Papoian GA (2018) AWSEM-IDP: a coarse-grained force field for intrinsically disordered proteins. *The Journal of Physical Chemistry B* **122**:11115-11125 https://doi.org/10.1021/acs.jpcb.8b05791 | PubMed

Wu Z, Cui Q, Yethiraj A. (2011) Driving force for the association of hydrophobic peptides: The importance of electrostatic interactions in coarse-grained water models. *The Journal of Physical Chemistry Letters* **2**:1794-1798 https://doi.org/10.1021/jz2006622

Wu Z, Cui Q, Yethiraj A. (2011) A new coarse-grained force field for membrane–peptide simulations. *Journal of Chemical Theory and Computation* **7**:3793-3802 https://doi.org/10.1021/ct200593t | PubMed

Yamada R, Takada S. (2023) Postsynaptic protein assembly in three and two dimensions studied by mesoscopic simulations. *Biophysical Journal* **122**:3395-3410 https://doi.org/10.1016/j.bpj.2023.07.015 | PubMed

Zhang Y, Li S, Gong X, Chen J. (2023) Toward accurate simulation of coupling between protein secondary structure and phase separation. *Journal of the American Chemical Society* **146**:342-357 https://doi.org/10.1021/jacs.3c09195 | PubMed

Zhang Z, Chan HS (2010) Competition between native topology and nonnative interactions in simple and complex folding kinetics of natural and designed proteins. *Proceedings of the National Academy of Sciences* **107**:2920-2925 https://doi.org/10.1073/pnas.0911844107 | PubMed

Zhou HX, Nguemaha V, Mazarakos K, Qin S. (2018) Why do disordered and structured proteins behave differently in phase separation?. *Trends in biochemical sciences* **43**:499-516 https://doi.org/10.1016/j.tibs.2018.03.007 | PubMed

Peer reviews

Reviewer #1 (Public review):

This manuscript is very interesting and timely. By introducing the critical effects of desolvation barriers and solvent (water)-separated minima into the implicit-solvent potentials (of mean force, PMFs) for coarse-grained molecular dynamics simulations of biomolecular liquid-liquid phase separation (LLPS), this work fills a gap that should be apparent to researchers of protein folding in the past couple of decades but has so far escaped deserved attention such that these basic features of aqueous solvation have seldom, though not never, been invoked in recent studies of biomolecular condensates. Although the present paper deals almost exclusively with homopolymers, this work can be a foundation for the future development of a new, more physical coarse-grained interaction scheme for simulating amino acid sequence-dependent effects, which I presume is the authors' ongoing or next endeavor. The results presented in this manuscript are highly valuable.

However, there is room for improvement in the authors' description of (i) the broader impact of effects of desolvation barrier and solvent-separated minimum in the thermodynamics of biomolecular condensates, especially with regard to the ramifications on hydrostatic pressure-dependent effects; (ii) the physical implication of using a 20-parameter hydropathy scale rather than a 210-parameter pairwise amino acid interaction scheme; and (iii) temperature-dependent effects, including the authors' discussion of "enthalpic" and "entropic" contributions. In all these aspects, the authors' discussion should be put in a more comprehensive context of the existing literature. At a few other places, the description of the methods and results should be clarified as well. Accordingly, the authors should revise the manuscript to address the following items thoroughly within the revised manuscript (not merely in the response letter) with the additional references mentioned below included in the revised discussion:

(1) In several places, e.g., on line 77 (p.2), the authors appear to suggest that "implicit-solvent representation" is the origin of the deficiency in commonly utilized coarse-grained potentials that this study is aiming to rectify. But desolvation barriers and solvent-separated minima are also features of implicit-solvent representations; they are just features that should be incorporated in more accurate implicit-solvent potentials. This point is stated quite clearly and accurately in the Abstract (p.1) but not consistently in the rest of the text. The authors should check the entire text carefully to ensure that a coherent, accurate perspective is presented.

(2) In the discussion of the importance of desolvation barriers and solvent-separated minima in the Introduction (pp.1-3), connections should be drawn to recent works that utilize these PMF features to rationalize hydrostatic pressure (P)-modulated effects on biomolecular LLPS,

including the P-dependent reentrant phase separation of alpha elastin; see Cinar et al. (2019) Chem Eur J 25:13049 (*https://chemistry-europe.onlinelibrary.wiley.com/doi/full/10.1002/chem.201902210*) and references therein, especially discussions around Figures 10, 11 & 13 in this reference.

(3) In the lower panels of Figures 2D, E (p.5), what do the differently colored small circles in the double-minimum free energy profiles represent? Does the color shading have the same meaning as that in the upper panels? If so, what do the positions of the circles on the free energy profile represent? The authors should clarify this.

(4) The discussion regarding entropy and enthalpy around Figure 2 is quite confusing as it stands. What do the authors mean exactly by the association of entropy or enthalpy with the desolvation barrier of the solvent-separated minimum? Are they referring to conformational entropy?

(5) Do the authors assume that the PMF (effective implicit-solvent potential) is a purely enthalpic term? It appears to be the authors' assumption. If so, the assumption has to be stated clearly in their discussion of "entropy" vs "enthalpy" around Figure 2.

(6) Closely related to points 3-5 above, it should be stated clearly that the "temperature" used in the authors' simulations does not represent experimental temperature if the authors are using purely enthalpic effective potentials because PMFs are in fact temperature-dependent. This clarification is necessary to avoid misunderstanding. In this regard, it should be noted that temperature-dependent effective interactions have been used for modeling biomolecular condensates in analytical theory (Lin, Song, Forman-Kay & Chan, J Mol Liq 2017, already in the citation list) as well as in coarse-grained molecular dynamics simulations [Dignon et al. (2019) ACS Cent Sci 5:821-830 (*https://pubs.acs.org/doi/10.1021/acscentsci.9b00102);* Chakravarti & Joseph (2025) Protein Sci 34:e70284 (*https://onlinelibrary.wiley.com/doi/10.1002/pro.70284)]*. The latter two studies, not cited currently, are particularly relevant and thus should be cited because the authors may wish to incorporate temperature-dependent features in their ongoing or future effort in constructing a more comprehensive coarse-grained interaction scheme for biomolecular LLPS simulation.

(7) In tackling "entropy" vs "enthalpy", it should be noted that the temperature dependence of the effective interactions entails an entropic contribution (which is itself temperature dependent) in addition to conformational entropy. As for the effective potential with desolvation barrier and solvent-separated minimum, it should be noted that the decomposition into entropic and enthalpic contributions at the direct contact, desolvation barrier, and solvent-separated minimum can be dramatically different, see, e.g., MaCallum et al. (2007) PNAS 104:6206-6210 (*https://www.pnas.org/doi/full/10.1073/pnas.0605859104*) and references therein.

(8) P.7, line 340: The proportionality relation follows directly from the standard Flory-Huggins result T_c = T chi(T)/chi_c, thus the proportionality constant is exactly 1/chi_c. Is this the standard relation that the authors are invoking here? The authors should clarify this.

(9) The study on dynamic consequences on pp.8-11 is interesting, but clarifications are necessary:

(i) The vertical schematic in Figure 4A should be explained in detail in its entirety. As it stands, no explanation is provided either in the figure caption or in the text. In particular, what does "elasticity driven" refer to?

(ii) The top snapshot in Figure 4A is labeled t_sim = 0 ns. Does it mean that the snapshot shown is the only chain configuration that the authors used to start the simulation, and that the snapshot does NOT represent the result of any time evolution, no matter how short the duration is? However, if that is the case, why is this snapshot identified with spinodal

decomposition if it is not the product of a time evolution from a more homogeneous configuration?

(iii) Related to (ii) - do the rectangular boxes shown represent the entire simulation box or just part of the box containing the polymer chains? One would imagine that if the top snapshot represents spinodal decomposition, the simulation would have been started at a more uniform distribution a short time prior? Why is this not the case?

(iv) What precisely do the small yellow beads and black-colored springs in the zoom-in image of Figure 4E represent?

(10) In discussing dynamic effects, it is useful to draw connections to related works on the effect of chain flexibility on "aging" of condensate [Biswas & Potoyan (2024) PRX 45:9222-9245 (*https://journals.aps.org/prxlife/abstract/10.1103/PRXLife.2.023011)]* and characterization of viscoelasticity in simulations of biomolecular condensates [Tejedor et al. (2023) J Phys Chem B 127:4441-4459 (*https://pubs.acs.org/doi/10.1021/acs.jpcb.3c01292)]*, as the effects of desolvation can be explored further based on these prior works.

(11) Much of the present study is based on the original HPS formulation of Dignon et al. (2018). In this regard and also in anticipation of future development of improved interaction schemes, several issues should be stated and discussed, even if briefly:

(i) The original HPS model has a basic shortcoming in accounting for the relative interaction strengths of, among others, arginine vs lysine residues [Das et al. (2020) PNAS 117:28795-28805 (*https://www.pnas.org/doi/10.1073/pnas.2008122117)]*.

(ii) Compared to 210-parameter pairwise interaction schemes, such as KH in Dignon et al. (2018) and Joseph et al. (2021), the 20-parameter interaction scheme is likely too restrictive to account for pairwise amino acid residue interactions [Wessén et al. (2022) J Phys Chem B 45:9222-9245 (*https://pubs.acs.org/doi/10.1021/acs.jpcb.2c06181)]*.

(iii) The height of the desolvation barrier may vary significantly for different amino acid residue pairs, see, e.g., Figure 11 of Cinar et al. (2019) mentioned above (and references therein). The authors should discuss these nuances in the revised version. They may also wish to take them into consideration in future investigations.

https://doi.org/10.7554/eLife.111124.1.sa2

Reviewer #2 (Public review):

Summary:

This manuscript addresses an important and timely question in the molecular simulation of biomolecular condensates. Most residue-level coarse-grained models used for IDP phase separation employ implicit solvent and represent effective interactions through relatively simple pairwise potentials. While these models have been very useful, they usually do not explicitly distinguish direct contacts from solvent-separated interactions, nor do they include an energetic barrier associated with water removal. This manuscript attempts to address that limitation by introducing desolvation-inspired terms into coarse-grained models and examining their consequences for phase behavior, chain conformations, dense-phase packing, and dynamics.

Strengths:

The central idea is physically well motivated. Using a simple homopolymer model, the authors show that increasing the desolvation barrier suppresses phase separation, whereas stabilizing solvent-separated contacts enhances phase separation. They further show that

solvent-separated interactions can reduce dense-phase over-compaction, which is a meaningful result given the known challenges in obtaining both accurate single-chain dimensions and realistic dense-phase properties from the same coarse-grained model. The finding that desolvation-like terms can reshape dense-phase packing without simply rescaling the overall interaction strength is interesting and could be useful for future model development. I also found the attempt to connect conformational changes across dilute and dense phases with thermal distance from the critical point to be intriguing. The dynamic analysis, including the FRAP-like simulations and the discussion of kinetic arrest during coarsening, adds another useful dimension to the work.

Weaknesses:

At the same time, there are several places where the manuscript would benefit from more careful framing. First, the desolvation terms are still effective coarse-grained parameters rather than a direct representation of water molecules. The language sometimes gives the impression that desolvation is being treated explicitly, whereas the model introduces desolvation-inspired effective interactions into an implicit-solvent framework. Second, the conformational analysis is interesting, but the broader context of prior work on dilute-to-dense phase conformational reorganization of IDPs could be more clearly discussed. This would help clarify what is new in the present work, whether it is the conformational change itself, its dependence on desolvation terms, or the proposed scaling with distance from the critical point. Third, the dynamic results are potentially useful, but the manuscript should more clearly articulate what is nontrivial beyond the expected slowing of local rearrangements by an added barrier in the potential.

Overall, I think this is a useful and potentially important contribution.

https://doi.org/10.7554/eLife.111124.1.sa1

Author response:

> ***Public Reviews:***
>
> ***Reviewer #1 (Public review):***
>
> *This manuscript is very interesting and timely. By introducing the critical effects of desolvation barriers and solvent (water)-separated minima into the implicit-solvent potentials (of mean force, PMFs) for coarse-grained molecular dynamics simulations of biomolecular liquid-liquid phase separation (LLPS), this work fills a gap that should be apparent to researchers of protein folding in the past couple of decades but has so far escaped deserved attention such that these basic features of aqueous solvation have seldom, though not never, been invoked in recent studies of biomolecular condensates. Although the present paper deals almost exclusively with homopolymers, this work can be a foundation for the future development of a new, more physical coarse-grained interaction scheme for simulating amino acid sequence-dependent effects, which I presume is the authors' ongoing or next endeavor. The results presented in this manuscript are highly valuable.*

We thank the reviewer for all the insightful comments.

> *However, there is room for improvement in the authors' description of (i) the broader impact of effects of desolvation barrier and solvent-separated minimum in the thermodynamics of biomolecular condensates, especially with regard to the ramifications on hydrostatic pressure-dependent effects; (ii) the physical implication of using a 20-parameter hydropathy scale rather than a 210-parameter pairwise amino acid interaction scheme; and (iii) temperature-dependent effects, including the authors'*

> *discussion of "enthalpic" and "entropic" contributions. In all these aspects, the authors' discussion should be put in a more comprehensive context of the existing literature. At a few other places, the description of the methods and results should be clarified as well. Accordingly, the authors should revise the manuscript to address the following items thoroughly within the revised manuscript (not merely in the response letter) with the additional references mentioned below included in the revised discussion:*
>
> *(1) In several places, e.g., on line 77 (p.2), the authors appear to suggest that "implicit-solvent representation" is the origin of the deficiency in commonly utilized coarse-grained potentials that this study is aiming to rectify. But desolvation barriers and solvent-separated minima are also features of implicit-solvent representations; they are just features that should be incorporated in more accurate implicit-solvent potentials. This point is stated quite clearly and accurately in the Abstract (p.1) but not consistently in the rest of the text. The authors should check the entire text carefully to ensure that a coherent, accurate perspective is presented.*

We thank the reviewer for the insightful comment and suggestion. In this work, rather than departing from the implicit-solvent modeling framework, our intention is to incorporate the desolvation effect within the implicit solvent model framework. In the revised manuscript, we will revise the text to ensure this point is presented clearly and consistently throughout the paper.

> *(2) In the discussion of the importance of desolvation barriers and solvent-separated minima in the Introduction (pp.1-3), connections should be drawn to recent works that utilize these PMF features to rationalize hydrostatic pressure (P)-modulated effects on biomolecular LLPS, including the P-dependent reentrant phase separation of alpha elastin; see Cinar et al. (2019) Chem Eur J 25:13049 (https://chemistry-europe.onlinelibrary.wiley.com/doi/full/10.1002/chem.201902210) and references therein, especially discussions around Figures 10, 11 & 13 in this reference.*

We thank the reviewer for bringing these references to our attention. The hydrostatic pressure modulated effects on LLPS provide important context for understanding the physical significance of desolvation barriers and solvent-separated minima. In the revised manuscript, we will expand the literature discussion by incorporating previous studies on pressure-modulated phase separation.

> *(3) In the lower panels of Figures 2D, E (p.5), what do the differently colored small circles in the double-minimum free energy profiles represent? Does the color shading have the same meaning as that in the upper panels? If so, what do the positions of the circles on the free energy profile represent? The authors should clarify this.*

We thank the reviewer for the suggestion to improve the clarity of the figure. In the lower panels of Figures 2D and 2E, the colored dots were intended solely as a qualitative illustration of the populations of residue-pair configurations along the effective energy surface. Their colors are not related to the color scale used in the phase diagrams shown in the upper panels. We will modify the color scheme to improve clarity.

> *(4) The discussion regarding entropy and enthalpy around Figure 2 is quite confusing as it stands. What do the authors mean exactly by the association of entropy or enthalpy with the desolvation barrier of the solvent-separated minimum? Are they referring to conformational entropy?*

We apologize for the confusion. When the desolvation barrier is high, configurations with inter-residue distances corresponding to the barrier region become difficult to access, thereby reducing the conformational entropy of the condensed phase. This interpretation is supported by Figure 2—figure supplement 1C, where increasing the desolvation barrier

decreases the population in the barrier region of the radial distribution function, indicating that fewer residue-pair configurations are sampled there. In contrast, increasing the depth of the solvent-separated minimum makes the condensed phase more energetically favorable. In the revised manuscript, we will incorporate this discussion to improve clarity.

> *(5) Do the authors assume that the PMF (effective implicit-solvent potential) is a purely enthalpic term? It appears to be the authors' assumption. If so, the assumption has to be stated clearly in their discussion of "entropy" vs "enthalpy" around Figure 2.*

We thank the reviewer for highlighting this important point. In this work, the PMF profile is constructed from atomistic simulation results, and thus both entropic and enthalpic contributions shape the overall PMF. In the revised manuscript, we will clarify that the PMF represents a free-energy profile along the intermolecular distance and therefore incorporates enthalpic and entropic contributions from the solute, solvent, and configurational degrees of freedom.

> *(6) Closely related to points 3-5 above, it should be stated clearly that the "temperature" used in the authors' simulations does not represent experimental temperature if the authors are using purely enthalpic effective potentials because PMFs are in fact temperature-dependent. This clarification is necessary to avoid misunderstanding. In this regard, it should be noted that temperature-dependent effective interactions have been used for modeling biomolecular condensates in analytical theory (Lin, Song, Forman-Kay & Chan, J Mol Liq 2017, already in the citation list) as well as in coarse-grained molecular dynamics simulations [Dignon et al. (2019) ACS Cent Sci 5:821-830 (https://pubs.acs.org/doi/10.1021/acscentsci.9b00102); Chakravarti & Joseph (2025) Protein Sci 34:e70284 (https://onlinelibrary.wiley.com/doi/10.1002/pro.70284)]. The latter two studies, not cited currently, are particularly relevant and thus should be cited because the authors may wish to incorporate temperature-dependent features in their ongoing or future effort in constructing a more comprehensive coarse-grained interaction scheme for biomolecular LLPS simulation.*

We thank the reviewer for raising this important point. We agree that PMFs and the corresponding effective interactions should be temperature dependent, and therefore the simulation temperature in our current temperature-independent CG potential cannot be interpreted as a fully quantitative experimental temperature. In the revised manuscript, we will clarify the above point. We will also expand the discussion to include previous studies that introduced temperature-dependent effective interactions in analytical theories and coarse-grained simulations of biomolecular condensates.

> *(7) In tackling "entropy" vs "enthalpy", it should be noted that the temperature dependence of the effective interactions entails an entropic contribution (which is itself temperature dependent) in addition to conformational entropy. As for the effective potential with desolvation barrier and solvent-separated minimum, it should be noted that the decomposition into entropic and enthalpic contributions at the direct contact, desolvation barrier, and solvent-separated minimum can be dramatically different, see, e.g., MaCallum et al. (2007) PNAS 104:6206-6210 (https://www.pnas.org/doi/full/10.1073/pnas.0605859104) and references therein.*

We agree that a temperature-dependent PMF includes entropic contributions beyond the configurational entropy discussed around Figure 2. In the present manuscript, our discussion of entropy in that context refers specifically to the reduced accessible configurational space of residue-pair states in the coarse-grained ensemble, rather than to a full thermodynamic decomposition of the PMF. In the revised manuscript, we will make this distinction explicit. We will also note that the direct-contact minimum, desolvation barrier, and solvent-separated minimum may each have distinct enthalpic and entropic components, and that resolving these components would require additional temperature-dependent PMF

calculations. We will discuss this as a limitation of the current model and as a direction for future parameterization.

> *(8) P.7, line 340: The proportionality relation follows directly from the standard Flory-Huggins result T_c = T chi(T)/chi_c, thus the proportionality constant is exactly 1/chi_c. Is this the standard relation that the authors are invoking here? The authors should clarify this.*

We thank the reviewer for pointing this out. Yes, our argument uses the condition that chi_c is fixed at the critical point for a given chain length. We will revise the text to explicitly state this relation and add the missing intermediate step, so that the proportionality used in the manuscript is clearer.

> *(9) The study on dynamic consequences on pp.8-11 is interesting, but clarifications are necessary:*
>
> *(i) The vertical schematic in Figure 4A should be explained in detail in its entirety. As it stands, no explanation is provided either in the figure caption or in the text. In particular, what does "elasticity driven" refer to?*
>
> *(ii) The top snapshot in Figure 4A is labeled t_sim = 0 ns. Does it mean that the snapshot shown is the only chain configuration that the authors used to start the simulation, and that the snapshot does NOT represent the result of any time evolution, no matter how short the duration is? However, if that is the case, why is this snapshot identified with spinodal decomposition if it is not the product of a time evolution from a more homogeneous configuration?*
>
> *(iii) Related to (ii) - do the rectangular boxes shown represent the entire simulation box or just part of the box containing the polymer chains? One would imagine that if the top snapshot represents spinodal decomposition, the simulation would have been started at a more uniform distribution a short time prior? Why is this not the case?*
>
> *(iv) What precisely do the small yellow beads and black-colored springs in the zoom-in image of Figure 4E represent?*

We thank the reviewer for pointing out these unclear issues in Figure 4. In the revised manuscript, we will better explain the vertical schematic in Figure 4A, including the progression from the early growth of density fluctuations, to intermediate kinetic arrest, and finally to late-stage coarsening. We will also clarify that “elasticity driven” refers to the resistance to domain deformation caused by transient inter-chain network connectivity. We will clarify that t_sim = 0 denotes the time immediately after the temperature quench from the high-temperature homogeneous state to the low-temperature two-phase region. This snapshot is the post-quench initial configuration, while spinodal decomposition refers to the subsequent amplification of density fluctuations after the quench. The displayed snapshot is one representative trajectory, not the only initial configuration used in the simulations. The quantitative kinetic analysis was averaged over multiple independent trajectories. The rectangular box represents the entire simulation box. Although the system was equilibrated at high temperature before the quench, instantaneous density fluctuations remain, so the initial configuration is not perfectly uniform. In Figure 4E, the yellow beads represent interacting residue pairs. The black springs schematically represent the transient elastic network formed by these interactions, rather than a precise structural model.

> *(10) In discussing dynamic effects, it is useful to draw connections to related works on the effect of chain flexibility on "aging" of condensate [Biswas & Potoyan (2024) PRX 45:9222-9245 (https://journals.aps.org/prxlife/abstract/10.1103/PRXLife.2.023011)] and characterization of viscoelasticity in simulations of biomolecular condensates [Tejedor et al. (2023) J Phys Chem B 127:4441-4459*

> *(https://pubs.acs.org/doi/10.1021/acs.jpcb.3c01292)], as the effects of desolvation can be explored further based on these prior works.*

We thank the reviewer for this helpful suggestion. In the revised Discussion, we will cite and discuss the related studies on condensate aging and viscoelasticity, including the effects of chain flexibility, sticker lifetime, desolvation, and transient network formation on condensate material properties. These works provide an important context for interpreting our dynamic results. We will clarify that desolvation may influence condensate dynamics not only by slowing local rearrangements, but also by modulating transient network connectivity, kinetic arrest, and viscoelastic relaxation.

> *(11) Much of the present study is based on the original HPS formulation of Dignon et al. (2018). In this regard and also in anticipation of future development of improved interaction schemes, several issues should be stated and discussed, even if briefly:*
>
> *(i) The original HPS model has a basic shortcoming in accounting for the relative interaction strengths of, among others, arginine vs lysine residues [Das et al. (2020) PNAS 117:28795-28805 (https://www.pnas.org/doi/10.1073/pnas.2008122117)].*
>
> *(ii) Compared to 210-parameter pairwise interaction schemes, such as KH in Dignon et al. (2018) and Joseph et al. (2021), the 20-parameter interaction scheme is likely too restrictive to account for pairwise amino acid residue interactions [Wessén et al. (2022) J Phys Chem B 45:9222-9245 (https://pubs.acs.org/doi/10.1021/acs.jpcb.2c06181)].*
>
> *(iii) The height of the desolvation barrier may vary significantly for different amino acid residue pairs, see, e.g., Figure 11 of Cinar et al. (2019) mentioned above (and references therein). The authors should discuss these nuances in the revised version. They may also wish to take them into consideration in future investigations.*

We thank the reviewer for highlighting these important limitations of the original HPS-based framework. We agree that a 20-parameter hydropathy-scale model has limitation in fully capturing residue-pair-specific interactions, including well-established differences such as those between arginine and lysine. In the revised manuscript, we will explicitly discuss this limitation and cite the suggested studies on residue-specific and pairwise interaction schemes. We also agree that desolvation barriers and solvent-separated minima are likely to depend on amino-acid pair identity. In the present work, we employ a simplified, residue-independent desolvation parameterization to isolate the general thermodynamic and kinetic consequences of desolvation in coarse-grained LLPS simulations. In the revised Discussion, we will clarify this scope and emphasize that developing residue-pair-specific desolvation parameters, potentially within a 210-parameter interaction framework, is an important direction for future work.

> ***Reviewer #2 (Public review):***
>
> *Summary:*
>
> *This manuscript addresses an important and timely question in the molecular simulation of biomolecular condensates. Most residue-level coarse-grained models used for IDP phase separation employ implicit solvent and represent effective interactions through relatively simple pairwise potentials. While these models have been very useful, they usually do not explicitly distinguish direct contacts from solvent-separated interactions, nor do they include an energetic barrier associated with water removal. This manuscript attempts to address that limitation by introducing desolvation-inspired terms into coarse-grained models and examining their consequences for phase behavior, chain conformations, dense-phase packing, and dynamics.*
>
> *Strengths:*

> *The central idea is physically well motivated. Using a simple homopolymer model, the authors show that increasing the desolvation barrier suppresses phase separation, whereas stabilizing solvent-separated contacts enhances phase separation. They further show that solvent-separated interactions can reduce dense-phase over-compaction, which is a meaningful result given the known challenges in obtaining both accurate single-chain dimensions and realistic dense-phase properties from the same coarse-grained model. The finding that desolvation-like terms can reshape dense-phase packing without simply rescaling the overall interaction strength is interesting and could be useful for future model development. I also found the attempt to connect conformational changes across dilute and dense phases with thermal distance from the critical point to be intriguing. The dynamic analysis, including the FRAP-like simulations and the discussion of kinetic arrest during coarsening, adds another useful dimension to the work.*

We thank the reviewer for all these positive and constructive assessment and comments. We are encouraged that the reviewer found the central idea physically well motivated and recognized the value of introducing desolvation-inspired terms to distinguish direct contacts, solvent-separated interactions, and the energetic barrier associated with water removal in coarse-grained models of biomolecular condensates.

> *Weaknesses:*
>
> *At the same time, there are several places where the manuscript would benefit from more careful framing. First, the desolvation terms are still effective coarse-grained parameters rather than a direct representation of water molecules. The language sometimes gives the impression that desolvation is being treated explicitly, whereas the model introduces desolvation-inspired effective interactions into an implicit-solvent framework.*

We agree that the current wording should more clearly reflect the nature of our model. The desolvation terms introduced in this work are effective coarse-grained interaction terms rather than an explicit molecular representation of water. In the revised manuscript, we will carefully revise the language throughout the article to describe the model as incorporating desolvation-inspired effective interactions within an implicit-solvent coarse-grained framework.

> *Second, the conformational analysis is interesting, but the broader context of prior work on dilute-to-dense phase conformational reorganization of IDPs could be more clearly discussed. This would help clarify what is new in the present work, whether it is the conformational change itself, its dependence on desolvation terms, or the proposed scaling with distance from the critical point.*

We appreciate this suggestion. In the revised manuscript, we will place the conformational analysis in the context of prior work and discuss the observed conformational changes more explicitly from the perspective of desolvation-inspired interactions. We will also clarify the assumptions behind the scaling relation between conformational change and thermal distance from the critical point.

> *Third, the dynamic results are potentially useful, but the manuscript should more clearly articulate what is nontrivial beyond the expected slowing of local rearrangements by an added barrier in the potential.*

We thank the reviewer for the suggestion. In the revised manuscript, we will clarify which aspects of the observed dynamics can be directly expected from the added desolvation barrier and which trends arise from the combined effects of desolvation on packing density, chain mobility, kinetic arrest, and coarsening.

We again thank the editors and reviewers for their constructive comments and suggestions. We believe that the planned revisions will improve the precision of the model description, clarify the physical interpretation of the desolvation-inspired terms, expand the relevant literature context, and better define the scope and limitations of the current framework.

https://doi.org/10.7554/eLife.111124.1.sa0